

**Physical Conditions in the Broad Line Region of $z \sim 3$
Quasars:
A Photoionization Method to Derive r_{BLR}**

C. Alenka Negrete¹ and Deborah Dultzin¹

Instituto de Astronomía, Universidad Nacional Autónoma de México, Mexico

Paola Marziani²

INAF, Astronomical Observatory of Padova, Italy

and

Jack Sulentic³

Instituto de Astrofísica de Andalucía, Spain

Received _____; accepted _____

To appear in ...

⁰Based on observations made with ESO Telescopes at Paranal Observatory under programme ID 078.B-0109(A)

¹anegrete@astrocu.unam.mx, deborah@astrocu.unam.mx

²paola.marziani@oapd.inaf.it

³sulentic@iaa.es

ABSTRACT

We present high S/N UV spectra for eight quasars at $z \sim 3$ obtained with VLT/FORS. The spectra enable us to analyze in detail the strongest emission features in the rest-frame range 1400-2000 Å of each source (CIII]λ1909, SiIII]λ1892, AlIIIλ1860, SiIIλ1814 and CIVλ1549). Previous work indicates that a component of these lines is emitted in a region with well-defined properties i.e., a high density and low ionization emitting region). Flux ratios AlIIIλ1860/ SiIII]λ1892, CIVλ1549/AlIIIλ1860 and SiIIλ1814/ SiIII]λ1892 for this region permit us to strongly constrain the electron density n_e and ionization parameter U through the use of diagnostic maps built from CLOUDY simulations. Reliable estimates of n_e and U allow us to derive the radius of the broad line region r_{BLR} from the definition of the ionization parameter. The r_{BLR} estimate and the assumption of virialized motions in the line emitting gas yields an estimate for black hole mass. We compare our results with estimates obtained from the $r_{\text{BLR}} -$ luminosity correlation customarily employed to estimate black hole masses of high redshift quasars.

Subject headings: galaxies: active — galaxies: high-redshift — quasars: general — quasars: emission lines

1. Introduction

1.1. Interpreting Quasar Spectra

Measuring relevant physical parameters from the observed broad-line spectra of quasars is still an open challenge. Identification and intensity measurements of the strongest emission lines has made possible a rough inference of the typical conditions of the emitting gas since the earliest days of quasar spectroscopy. The very first quasars of intermediate redshift discovered in the 1960s showed a fairly high ionization spectrum, with prominent lines of C^{IV}λ1549, and He^{II}λ1640 in addition to strong Balmer lines of the low-redshift quasars. Photoionization by the central continuum source was considered the preeminent heating mechanism of the emitting gas. Significant C^{III}]λ1909 emission suggested electron density (n_e) in the range $10^9 - 10^{10} \text{ cm}^{-3}$. The observed intensity ratio C^{III}]λ1909/C^{IV}λ1549 indicated ionization parameter (defined by Eq. 1 later in this paper) values of the order of 10^{-1} . This photoionization scenario is successful in explaining at least some quasar optical and UV spectra (see the review by Davidson and Netzer 1979 for a synopsis). More recent work emphasized the existence of several problems with this simple scenario. Low ionization lines (LILs), and especially Fe^{II} are too strong to be explained by a photoionized region of moderate density and column density (see for example Dumont and Mathez 1981; Joly 1987; Collin-Souffrin et al. 1988; Dumont and Collin-Souffrin 1990). These authors stressed that the LILs required a denser, low-temperature environment.

We unfortunately lack a simple well-defined diagnostic measure of physical conditions in the broad line region. One strategy for estimating electron density

in astrophysical sources involves using two emission lines of the same ion, and with similar energies above the ground level, but with different radiative transition probabilities A . In practice one often chooses two lines from the same term where one forbidden/semi-forbidden transition is associated with another that is semi-forbidden/permitted in order to ensure very different values of A (for example, [SiIII] λ 1882 and [SiIII] λ 1892). This technique is not straightforwardly applicable to the broad lines of quasars, precisely because the lines are broad, suitable candidates are too closely spaced in wavelength, and density is at least an order of magnitudes higher than the critical density for the forbidden transitions used in spectra of planetary nebulae and HII regions. In addition the S/N and the resolution of quasar spectra are usually not very high.

Feibelman and Aller (1987) used the CIII] λ 1909/ [SiIII] λ 1892 ratio to study the rather high-density environment typical of symbiotic stars ($n_e \sim 10^{7-10} \text{ cm}^{-3}$). In this case we have two semi-forbidden (intercombination) resonance lines with significantly different transition probabilities (see Table 1). The lines are emitted by two iso-electronic species with somewhat different ionization potentials (24 eV for C⁺ vs. 16 eV for Si⁺). The ionic fraction is dependent on the relative abundance of silicon-to-carbon (to be assumed) as well as on the ionization structure within the emitting region (to be computed). Using lines of different ions introduces additional potentially serious sources of uncertainty. It is perhaps not surprising that most workers believe that n_e in the BLR cannot be reliably estimated using quasar spectra. Strong CIII] λ 1909 emission would imply that n_e cannot be very high ($n_e \sim 10^{11-13} \text{ cm}^{-3}$). Very high density was invoked to explain the rich low ionization spectrum (especially FeII) seen in the spectra of most quasars. Several

lines in the UV spectrum of I Zw 1 point towards high density at least for the LIL emitting zone: prominent FeII, relatively strong AlIII λ 1860, and detection of CIII λ 1176 (Laor et al. 1997b). The region where these lines are produced cannot emit much CIII λ 1909. But is CIII λ 1909 really so strong in most quasars? BLR conditions are certainly complex and a single emitting region is not sufficient to explain both LILs and high ionization lines (HILs).

1.2. Quasar Systematics

Quasar spectra are not all alike. There are significant differences in line intensity ratios and broad line profiles from object to object (Bachev et al. 2004; Marziani et al. 2010). More importantly, these differences can be organized in a systematic way as has been realized since the early 1990s (Boroson and Green 1992). Since then several authors stressed the importance of the so-called eigenvector 1 (E1) of quasars (e.g. Gaskell et al. 1999). Sulentic et al. (2000, 2007) expanded the E1 trends into a 4-dimensional space involving optical, UV and X-ray measures. They also defined spectral types along a sequence occupied by AGN an optical plane involving FeII and FWHM $H\beta$ parameters. Objects at extreme ends of the E1 sequence are very different at almost all wavelengths and median spectra computed in spectral bins within this plane emphasize systematic changes in broad line properties (Sulentic et al. 2002, 2007). The differences have motivated the suggestion of a possible dichotomy between narrow line Seyfert 1 (NLSy1s) like sources and broader line objects that include almost all radio-loud quasars. The most effective divider of the two quasar types appears to be FWHM ($H\beta_{BC}$) \approx

4000 km s⁻¹ for low-to-moderate luminosity sources (Marziani et al. 2009). This corresponds to $L/L_{\text{Edd}} \sim 0.2 \pm 0.1$ (Marziani et al. 2003b).

The distinction between NLSy1-like objects (hereafter Population A sources) and the rest of quasars (Population B) is of special relevance here. Pop. A sources show relatively low equivalent width lines with e.g. the $\lambda 1900$ blend $\sim 30 \text{ \AA}$. A close analysis of the CIII] $\lambda 1909$ blend in the prototypical NLSy1 I Zw 1 shows strong SiIII] $\lambda 1892$, and AlIII] $\lambda 1860$ blended with rather weak CIII] $\lambda 1909$ along with prominent FeIII and FeII blends (Laor et al. 1997b; Vestergaard and Wilkes 2001). The CIII] $\lambda 1909$ line is apparently so weak that FeIII] $\lambda 1914$ may be the most prominent feature at $\lambda \approx 1910 \text{ \AA}$. This interpretation is confirmed by detailed deblending of a source (SDSS J120144.36+011611.6) that can be considered a high luminosity analog of I Zw 1 (§6.1).

I Zw 1, although extreme, is not unique as a NLSy1. Median composite UV spectra of low- z quasars show that AlIII] $\lambda 1860$ and SiIII] $\lambda 1892$ are more prominent in 4DE1 spectral types A2 and A3 (I Zw 1 belongs to the latter, Bachev et al. 2004). A significant number of extreme NLSy1 are not classified as quasars in SDSS and must be collected from the galaxy catalog (Hu et al. 2008).

1.3. Emission Line Diagnostics and BLR Properties

Emission lines and line ratios are used in diagnostic maps to estimate temperatures and electronic densities in galactic and extragalactic photoionized regions. Examples include HII-regions and galaxies with HII-region nuclear spectra

where electron densities are less than $n_e \approx 10^4 \text{ cm}^{-3}$. This method has been successfully applied to the narrow line region (NLR) in AGN. Application to the broad line quasars has yielded results that are difficult to interpret. One exception is the recent work by Matsuoka et al. (2008) who succeeded in analyzing the partly ionized region thought to emit most of the LILs in quasar spectra. They suggest that OI 8446 and the CaII triplet are emitted by dense, low ionization gas probably located in the periphery of the BLR. If the electron density and ionization conditions are known it is possible to derive, with additional assumptions, the distance of the BLR emitting region from the central continuum source.

The physical conditions of photoionized gas can be described by electron density n_e , column density N_c , metallicity (normalized to solar), shape of the ionizing continuum, and the ionization parameter U . The latter represents the dimensionless ratio of the number of ionizing photons and n_e . Both U and n_e are related through the equation

$$U = \frac{\int_{\nu_0}^{+\infty} \frac{L_\nu}{h\nu} d\nu}{4\pi n_e c r^2} \quad (1)$$

where L_ν is the specific luminosity per unit frequency, h is the Planck constant, ν_0 the Rydberg frequency, c the speed of light, and r can be interpreted as the distance between the central source of ionizing radiation and the line emitting region. If we know *the product of* n_e and U , we can estimate the radius r of the BLR from this relationship. The dependence of U on r_{BLR} was used by Padovani & Rafanelli (1988) to derive central black hole masses assuming a plausible average value of the product $n_e \cdot U$. The typical value of n_e was derived at that time from semiforbidden line CIII] λ 1909 which implied that the density could not be much higher than log

$n_e \approx 10^{9.5} \text{ cm}^{-3}$ (Osterbrock & Ferland 2006). Padovani (1988) derived an average value $\langle U \cdot n_e \rangle \approx 10^{9.8}$ from several sources where r_{BLR} had been determined from reverberation mapping, and for which the number of ionizing photons could be measured from multiwavelength observations. The average value was then used to compute black hole masses for a much larger sample of Seyfert 1 galaxies and low- z quasars (Padovani & Rafanelli 1988; Padovani, Burg & Edelson 1989). We are unaware of any systematic applications of this photoionization method in more recent times. Wandel, Peterson & Malkan (1999) compared the results of the photoionization method with the ones obtained through reverberation mapping, found a very good correlation for the masses computed with the two methods, and concluded that “both methods measure the mass of the central black hole.”

1.4. Outline of the paper

The importance of the product $U \cdot n_e$ goes beyond knowledge of the physical conditions in the BLR if it can lead to independent estimates of BLR radius and black hole mass. This paper identifies suitable emission line ratios that overcome some of the major problems in the analysis of emission lines of quasars. It also defines a photoionization method that can be applied to even the highest redshift quasars making use of high S/N near-IR spectroscopic data. In §2 we present the spectra of 8 pilot sources obtained with the VLT/FORS; in §3 we discuss data reduction; In §4 we describe our method of fitting broad emission line profiles; in §5 we give a phenomenological interpretation of the profile fits; in §6 we describe a method for deriving BLR physical conditions and give the results of our fits; in §7

we discuss two sources not belonging to our sample that show extreme behavior; in §8 we derive the radius of the BLR (its distance from the ionizing source) and the mass of the black hole for each quasar in our sample; in §9 we compare our results with previous estimates; finally, in §10 we summarize our results and the prospect of a more extended application of our method. All the computations were made considering $H_0 = 70 \text{ km s}^{-1} \text{ Mpc}^{-1}$ and a relative energy density $\Omega_\Lambda = 0.7$ and $\Omega_M = 0.3$.

2. Observations

Data were obtained between Nov. 2006 and Jan. 2007 using the VLT2/FORS1 telescope operated in service mode. FORS1 is the visual and near UV focal reducer and low dispersion spectrograph of the Very Large Telescope (VLT) operated by European Southern Observatory (ESO) (Appenzeller et al. 1998). Our VLT sample consists of 8 quasars with $z \sim 3$. In Figure 1 we show the spectra uncorrected for redshift. Tab. 2 provides a log of observations that is organized as follows.

Column 1: object name, Col. 2: apparent B magnitude, Col. 3 redshift, Col. 4: line(s) used for redshift estimation: a) $\text{O I } \lambda 1304.8$, b) $\text{C III }] \lambda 1909$; Col. 5: absolute B magnitude, computed for $H_0 = 70 \text{ km s}^{-1} \text{ Mpc}^{-1}$, Col. 6 flux at 6 cm taken from FIRST (Far InfraRed and Submillimetre Telescope), Col. 7: date (refers to time at start of exposure), Col. 8: Digital Integration Time, Col. 9: number of exposures with integration time equal to DIT, Col. 10: airmass at the beginning of each exposure, Col. 11 S/N in the continuum around 1700 \AA .

One of our quasars J00521-1108 yielded only a low S/N spectrum which we retained because observed features in the blend at $\sim 1900 \text{ \AA}$ are clear enough to fit the individual lines. Two more sources, J01225+1339 and J02287+0002, are BAL quasars. We will keep them separate because $\text{CIV}\lambda 1549$ is severely affected by absorption.

3. Data Reduction

Data were reduced using standard IRAF tasks. All spectra were wavelength and flux calibrated in the observed frame and then corrected for Galactic extinction. Flux correction was applied using meteorological data provided by ESO. The observed flux was multiplied by the inverse of the light lost computed from the ratio seeing over slit width in arcsec. Correction to rest frame requires estimating the redshift z which is not a trivial task as outlined below. Rest frame correction also involved scaling the fluxes by a factor $(1+z)^3$. Measurements were carried out on the rest-frame spectra. It is necessary to describe below two important aspects of the data reduction.

3.1. A & B Atmospheric Bands Correction

The A or B atmospheric band falls on top of the 1900\AA blend in many of the spectra. This is an important region for this study especially because it involves $\text{SiIII}\lambda 1892$, $\text{AlIII}\lambda 1860$, and $\text{SiII}\lambda 1814$. In order to remove these absorption features we created an A+ B band template from standard star spectra used as specific flux

calibrators. We scaled this template to find a best fit. Fig. 1 shows the A and B absorption correction where we make a line identification to illustrate which lines are affected. In cases where the A or B bands overlap a weak line like SiII λ 1814 the effect is considerable and measures of SiII λ 1814 should not be considered at all or with extreme care. This happens for sources J00521-1108, J03036-0023, and J20497-0554. In cases where one of the bands overlaps a stronger line like SiIII] λ 1892 or AlIII] λ 1860, the correction was good enough to permit accurate measures.

3.2. Redshift Estimate

Normally one uses strong narrow emission lines to set the rest frame in a quasar. In our case no strong narrow lines are available so we consider the peaks of Ly α , CIV λ 1549 and CIII] λ 1909. The Ly α peak is affected by absorption and CIV λ 1549 is a HIL feature often showing blueshifts and/or asymmetries (Gaskell 1982, Espey et al. 1989, Corbin 1990, Tytler & fan 1992; Marziani et al. 1996; Richards et al. 2002, Baskin & Laor 2005; Sulentic et al. 2007). This is especially true in Pop. A sources which predominate in our sample. CIII] λ 1909 is blended with SiIII] λ 1892 and FeIII that is especially prominent in this region and could well affect the peak. Pop. B sources show a rather weak Fe spectrum making the CIII] λ 1909 peak a more reliable z estimator.

Our best option is to use the low ionization line OI λ 1304 when it is strong. However it is blended with low ionization SiII $\lambda\lambda$ 1304,1309 ($^2P_{3/2,1/2}^0 - ^2S_{1/2}$). Both OI λ 1304 and SiII $\lambda\lambda$ 1304,1309 are broad lines and in Pop. B sources might show

large redshifts or even significant blueshifts. Simulations in the (n_e, U) region of interest show $O\text{I}\lambda 1304 \approx 2 \text{ SiII}\lambda 1308$ and this is confirmed in the spectrum I Zw 1 where $O\text{I}\lambda 1304$ and $\text{SiII}\lambda\lambda 1304, 1309$ are resolved. The two components of the $\text{SiII}\lambda\lambda 1304, 1309$ doublet are set to the same intensity (i.e., we assume an optically thick case). Modelling the blend with 5 Gaussians (the three components of the OI feature are produced by Bowen fluorescence mechanism, and should show ratios consistent with their transition probabilities. Generating a model spectrum in IRAF (lines broadened to 4000 km s^{-1}) yields a rest frame peak wavelength of $1304.8 \pm 0.2 \text{ \AA}$ (in vacuum) which we use as a reference for our VLT spectra assuming that there is no hint of systematic BC shifts as is the case for all Pop. A sources (the majority in our sample) and many Pop. B sources (Marziani et al. 2003a).

Examination of Fig. 2 reveals that the peak of $O\text{I}\lambda 1304$ in sources J00521-1108 and J02390-0038 is not observed clearly. We use $\text{CIII]}\lambda 1909$ to set the rest frame in these two sources. There are three other sources J00103-0037, J02287+0002 and J20497-0554 where the redshift estimation using both $O\text{I}\lambda 1304$ and $\text{CIII]}\lambda 1909$ are not in good agreement. The largest disagreement we found was for J02287+0002 for which we show two fits, one for each restframe (Fig. 7). This represents a source of error in the determination of line intensities especially for $\text{CIV}\lambda 1549$ because if the peak is shifted, then the major contribution would likely involve the blueshifted component, instead of the core broad component. Redshifts obtained for the three remaining quasars, J01225+1339, J03036-0023 and J23509-0052, were obtained from $O\text{I}\lambda 1304$. Fig. 3 shows the deredshifted VLT-FORS spectra for our sample of 8 quasars.

4. Data Analysis

4.1. Methodological Considerations on Multicomponent Fits

The SPECFIT IRAF task (Kriss 1994) allows us to fit the continuum, emission and absorption line components, FeII and FeIII blends, etc. We fit two spectral ranges: 1) 1450–1680 Å for analysis of C IV λ 1549 and 2) 1750–2050 Å for analysis of the 1900 Å blend. Significant FeII and FeIII emission are expected close to and underlying the 1900 Å blend. Study of the 1900 Å blend is especially difficult in quasars because the lines are broad and the blending severe. We therefore need to take advantage of several previous results.

4.2. FeII and FeIII Emission

Our approach is completely empirical and employs an FeII + FeIII template taken from templates successfully used in previous works. Our FeII template is based on a CLOUDY simulation and is not very far from the preferred model of Bruhweiler & Verner (2008).

FeIII lines are common and strong in the vicinity of C III] λ 1909 as is evidenced by their presence in average LBQS (Francis et al. 1991) and SDSS (Vanden Berk et al. 2001) spectra. Vestergaard & Wilkes (2001) produced an FeIII template based on the UV spectrum of IZw1. Since then, Sigut et al. (2004) have modeled the FeIII BLR spectrum. See also Verner et al. (2003) for a plot of emission around 1800 Å. Ly α pumping enhances FeIII λ 1914 (Johansson et al. 2000) and this line can be a major contributor to the C III] λ 1909 blend (see Fig. 2 of Vestergaard & Wilkes).

We reproduced the empirical FeIII template of Vestergaard & Wilkes (2001), taking advantage of the line identifications from Ekberg (1993). When detected we can use FeII UV 191 to set a rough FeII level while the feature at 2080 Å is helpful for a more precise estimation of the intensity of FeIII. The continuum was fitted using the regions around 1450Å (1750 and 1960Å) that are relatively free of FeII emission (Vanden Berk et al. 2001). We used the same power-law to describe the continuum at both the CIVλ1549 and 1900Å regions.

4.3. Line Components

We base our `specfit` analysis on several previous observational results. The most important ones are as follows:

- Sulentic et al. (2002) gridded the FWHM $H\beta$ versus R_{FeII} parameter plane into bins of fixed $\Delta \text{FWHM} = 4000 \text{ km s}^{-1}$ and $\Delta R_{\text{FeII}} = 0.5$. Quasar spectra in different bins are different in many measures beyond these grid intervals. The largest differences are found between NLSy1-like objects with $\text{FWHM}(H\beta) \leq 4000 \text{ km s}^{-1}$ (called Population A) and broader sources with $\text{FWHM}(H\beta) \gtrsim 4000 \text{ km s}^{-1}$ (Population B) respectively. This gridding is valid for low z (< 0.7) quasars. At higher z an adjustment must be made since no sources with $\text{FWHM } H\beta < 3500 \text{ km s}^{-1}$ above redshift $z \sim 3$ (Marziani et al. 2009).
- Median spectra were computed for spectral bins from the atlas of Marziani et al. (2003a) who found that $H\beta$ can be described by a Lorentz function in

Pop. A sources and by the sum of 2 Gaussians in Pop. B sources (unshifted + broader redshifted components) (Zamfir et al. 2010; Marziani et al. 2010).

- A careful FeII subtraction reveals a blue-shifted $H\beta$ component in some bin A3 sources (i.e. the strongest FeII emitters).
- C IV $\lambda 1549$ (HIL) and $H\beta$ (LIL) profiles show significant differences in Pop. A. Large ($\lesssim -1000$ km s $^{-1}$) C IV $\lambda 1549$ blueshifts are observed in Pop. A *only* (Sulentic et al. 2007). HIL and LIL profiles are more similar in Pop. B sources.
- We do not have $H\beta$ observations for our high- z objects since there are no near IR spectra. We use the results of Marziani et al. (2003b,2010): they show that the broad components (BC) of Si III $\lambda 1892$, Al III $\lambda 1860$ and C IV $\lambda 1549$ lines are similar to those of $H\beta$, including the FWHM and profile shapes, either Gaussian or Lorentzian. The similarity helps us to define whether an object is Population A or B in this paper.

These observational results point toward three different components in broad line profiles (see Marziani et al. 2010) which can be described as follows:

1. A broad component (BC) showing a roughly symmetric profile with FWHM in the range 1000-5000 km s $^{-1}$. It is consistent with the component identified by Matsuoka et al. (2008). This broad component dominates LILs in Balmer lines of Pop. A sources while it becomes less prominent in Pop. B. The profile is best modeled by a Lorentzian function in Pop. A sources while Pop. B profiles are better described by a Gaussian (Marziani et al. 2003b).

2. A very broad component (VBC) is seen in LILs and HILs of most pop B sources but is absent from Pop. A profiles. The VBC can be modeled as a Gaussian ($\text{FWHM} \sim 10000 \text{ km s}^{-1}$) often with a significant shift to the red. It can be called a defining property of Pop. B sources (Marziani et al. 2010).
3. A blueshifted broad component (BBC), defined as the residual emission in the $\text{CIV}\lambda 1549$ line after subtracting a scaled BC Lorentzian profile (Marziani et al. 2010). We model this profile as a blueshifted Gaussian. The Gaussian approximation is probably inappropriate especially if the BCC is strong: this component is believed to be produced in a partially-obscured radial flow, not in a virialized emitting system. This blueshifted component is often prominent in $\text{CIV}\lambda 1549$ and $\text{Ly}\alpha$ of Pop. A sources. It is much less intense in Pop. B sources.

4.4. Errors

We identify five sources of error from the conditions for data reduction and methodological considerations described above:

1. A & B atmospheric bands correction (already described in §3.1).
2. Line profile shape, Gaussian or Lorentzian (Pop. A or B). The distinction between Pop. A and B is based on line width with the boundary at $\text{FWHM H}\beta \approx 4000 \text{ km s}^{-1}$ in low luminosity quasars and around $\approx 5000 \text{ km s}^{-1}$ at higher luminosity such as the eight sources presented here. Some quasars are unambiguously Pop. A or B because of line width and because Pop. B sources

show an $H\beta$ VBC and pop A sources a prominent CIV BBC. In these cases only one profile shape (Gaussian or Lorentzian) was fitted. However, source J23509-0052 is not easily classified Pop. A or B. In such ambiguous case we tried both Gaussian and Lorentzian fits.

3. Rest-frame determination using $O\text{I}\lambda 1304$ or $\text{C}\text{III}]\lambda 1909$. Sometimes the redshift estimates derived from the two lines do not agree, most likely because of absorptions present in $O\text{I}\lambda 1304.8$ and because this is not a very intense line. The principal impact of uncertainty in the rest frame placement is estimation of the wavelength of $\text{C}\text{IV}\lambda 1549$. If the peak of the line profile differs from $\lambda 1549\text{\AA}$, the BC intensity is diminished and we infer a greater contribution from the blue (BBC) component. Similarly, for the blend 1900\AA , the rest frame shift may increase or decrease our estimate for the strength of $\text{C}\text{III}]\lambda 1909$ with consequent decrease or increase of the $\text{Si}\text{III}]\lambda 1892$ contribution. This additional source of uncertainty affects J00103-0037, J02287+0002 and J20497-0554.
4. FeII intensity (continuum placement). Broad FeII emission can produce a pseudo-continuum affecting our estimates of emission line intensities. $\text{Si}\text{II}\lambda 1814$ is especially affected in our spectra because it is weak. $\text{Al}\text{III}\lambda 1860$ is similarly affected when it is weak. The effect is less noticeable for $\text{C}\text{IV}\lambda 1549$ since expected FeII emission underlying the $\text{C}\text{IV}\lambda 1549$ line is weak.
5. Broad absorption lines in BAL quasars principally affect the blue side of $\text{C}\text{IV}\lambda 1549$. We also find an absorption feature between $\text{Fe}\text{II}\lambda 1787$ and $\text{Si}\text{II}\lambda 1814$ (eg. Fig. 7, (b) panels). In sources J01225+1339 and J02287+0002

we can only set upper limits for line intensities (since we fit unabsorbed components).

There are other sources of error such as small BC shifts and FWHM variations. We assume that UV broad components lines ($\text{SiIII}\lambda 1892$, $\text{AlIII}\lambda 1860$, $\text{SiII}\lambda 1814$ and $\text{CIV}\lambda 1549$) have the same FWHM and shift, although we let variations within different fits (i.e. fits assuming gaussian or lorentzian profiles or different continuum placement).

The goal of this study is to estimate diagnostic line ratios. A posteriori, we can say that the estimated line ratios are rather insensitive to the emission component profile shape: assuming a Gaussian or Lorentzian profile yields the same ratio for the strongest lines (i.e., $\text{CIV}\lambda 1549$, $\text{SiIII}\lambda 1892$, $\text{AlIII}\lambda 1860$) upon which our analysis is based (with an uncertainty of $\sim 10\%$). The same considerations apply to the redshift uncertainty. The most serious sources of error remain effects of A/B band overlap for $\text{SiII}\lambda 1814$ and the presence of a BAL for $\text{CIV}\lambda 1549$.

5. Results of Line Component Analysis on Individual Objects

In Figures from 4 to 7 we show our best fits for the VLT sample taking into account the considerations described in §4. We present here a phenomenological description of the fits. In some objects the line profiles, intensities and line ratios follow the trends of Pop. A or B sources, but in some other objects the classification remains uncertain. In all broad emission lines of all sources we are looking for evidence of three possible components as described above: BC, VBC and BBC.

- J00103-0037 – This source resembles a Pop. B quasar on the basis of comparison with sources along the 4DE1 sequence. Specifically we cite the prominent CIII]λ1909 emission and weak (but detected) AlIIIλ1860 (Fig. 5(1b)). FeII appears to be present as evidenced by an appreciable “bump” at 1780 Å(UV 191). Fainter FeII emission is relatively unimportant because FeII creates a pseudo-continuum. SiIIλ1814 is compromised by A band absorption. The red side of CIVλ1549 is blended with HeIIλ1640. Fitting a BC with no shift (with a FWHM(BC)~4700 kms⁻¹ derived from AlIIIλ1860 + a blueshifted broad component (BBC) to CIVλ1549 leaves a very large residual on the red side. A VBC component is needed to model the spectrum (Fig.5 (1a)) and that confirms it to be a Pop. B squasar (Marziani et al. 2009). The blend at 1900Å includes a CIII]λ1909 VBC and the fit indicates CIVλ1549/CIII]λ1909 (VBC) ≈ 7 which is reasonable.
- J00521-1108 – This pop. B source shows the noisiest spectrum in the sample. Absorption features seriously affect the CIVλ1549 profile (Fig. 5(2a)). We fit a FWHM(BC) ~ 6200 km s⁻¹ with CIVλ1549 requiring a large VBC to account for the red wing. Residuals on the red side of CIII]λ1909 also point toward a considerable CIII]λ1909VBC contribution (Fig. 5(2b)). AlIIIλ1860 is weak consistent with pop. B.
- J02390-0038 – This source also appears to be a Pop. B source. Consistent with this classification we find FeIIλ1780 to be weaker than SiIIλ1814. FWHM(BC)~ 7000 km s⁻¹. CIII]λ1909 is prominent and shows a small red wing indicating VBC emission. The A band absorption lies between

SiIII] λ 1892 and AlIII λ 1860 (Fig. 5(3b)) making it possible that we are overestimating AlIII λ 1860. Figure 5(3a) shows CIV λ 1549 with a slightly redshifted peak, a moderate blue-shifted component and a weak VBC.

- J03036-0023 – This Pop. A source shows a clear inflection between CIII] λ 1909 and SiII λ 1814 (Fig. 4(1b)). We estimate FWHM(BC) \sim 3500 km s $^{-1}$ and require a Lorentzian function to fit the two lines. There is no evidence for a VBC in CIII] λ 1909. AlIII λ 1860 is prominent. Unfortunately the blue wing of SiII λ 1814 and the red wing of FeII λ 1780 are affected by A band absorption. The peak of CIV λ 1549 is blueshifted and requires a strong BBC and weak BC (Fig. 4(1a)).
- J20497-0554 – This Pop. A source shows FWHM(BC) \sim 3600 km s $^{-1}$ which is equivalent to \sim 1000 km s $^{-1}$ at low redshift making this source a likely a high z NLSy1. We see a prominent AlIII λ 1860 line and FeII λ 1780 (Fig. 4(2b)). SiIII] λ 1892 is affected by several narrow absorption lines, however it is obviously intense. The lack of a red wing on CIII] λ 1909 suggests that no VBC is present. As for J03036-0023, the CIV λ 1549 line can be accounted for by an unshifted BC (assumed Lorentzian) of a considerably contribution of a BBC (Fig. 4(2a)).
- J23509-0052 – This is likely a source near the Pop. A-B boundary with FWHM(BC) \sim 4500 km s $^{-1}$. The contribution of FeII is small and FeII λ 1780 is weak (Fig. 6(2b)). CIII] λ 1909 shows a small red wing that implies a weak VBC. AlIII λ 1860 is not prominent but its contribution to the blend is very clear and can be reasonably well estimated. CIV λ 1549 shows a slight blue

asymmetry with a BBC (Fig. 6(2a)) required to model it. We also see a contribution of $\text{HeII}\lambda 1640$ BBC and a not very strong $\text{CIV}\lambda 1549$ VBC.

There are also two BAL quasars in our sample.

- J01225+1339 – $\text{CIV}\lambda 1549$ is highly affected by two broad absorption lines (Fig. 7(1a)) with blueshifts of 5200 and 10800 km s^{-1} at peak absorption with equivalent widths/FWHM $-12\text{\AA} / 3900 \text{ km s}^{-1}$ and $-25\text{\AA}/5200 \text{ km s}^{-1}$, respectively. The blueshift of the $\text{CIV}\lambda 1549$ peak leads us to suspect a large blueshifted BBC emission component. The 1900 \AA blend shows absorptions coincident with $\text{FeII}\lambda 1780$ and the blue side of $\text{SiII}\lambda 1814$ which is however unambiguously detected (Fig. 7(1b)). $\text{AlIII}\lambda 1860$ is prominent which implies that this a Pop. A source. The $\text{FWHM(BC)} \sim 4300 \text{ km s}^{-1}$ is consistent with a high luminosity Pop. A source. The $\text{CIII]}\lambda 1909$ is well fitted with a Lorentzian profile and a VBC is not needed. Broad A band atmospheric absorption lies over $\text{SiIII]}\lambda 1892$.
- J02287+0002. The estimated rest frame of this quasar differs by $\sim 1400 \text{ km s}^{-1}$ using $\text{OI } \lambda 1304$ and $\text{CIII]}\lambda 1909$. This is the largest discrepancy in our sample. In order to evaluate the effect of the z discrepancy we performed two fits using both rest frames. Figs. 7(2a) and (2b) use the $\text{CIII]}\lambda 1909$ restframe. In the 1900 \AA blend, we found a contribution of $\text{SiIII]}\lambda 1892$ similar to $\text{CIII]}\lambda 1909$. If we use the $\text{OI}\lambda 1304$ inferred rest frame we show in Figs. 7(2a*) and (2b*) that $\text{CIII]}\lambda 1909$ becomes stronger with a resultant decrease of $\text{SiIII]}\lambda 1892$. A similar effect occurs for $\text{CIV}\lambda 1549$ broad and blue-shifted

components. The C^{IV}λ1549 BAL shows a blueshift of 9100 km s⁻¹ at deepest absorption, a EW of -14 Å and a FWHM of 4600 km s⁻¹. The FWHM(BC) ~ 5700 km s⁻¹ is not consistent with Pop. A but this object shows features that are typical of extreme Pop. A sources: prominent Fe^{II}λ1780, strong Al^{III}λ1860, no C^{III}]λ1909 VBC. It is likely that this BAL QSO is an outlier like Mark 231 at low-*z* (Sulentic et al. 2006).

6. Estimation of Physical Conditions in the Emitting regions

6.1. CLOUDY Simulations

We computed a multidimensional grid of CLOUDY (Ferland et al. 1998) simulations, (see also Korista et al. 1997) to derive U and n_e from our spectral measurements. Simulations span the density range $7.00 \leq \log n_e \leq 14.00$, and $-4.50 \leq \log U \leq 00.00$, in intervals of 0.25. Each simulation was computed for a fixed ionization parameter and density assuming plane parallel geometry. The 2D grid of simulations was repeated twice assuming $N_c = 10^{23}$ and 10^{24} cm⁻². Several cases were computed also for $N_c = 10^{25}$ cm⁻². Metallicity was assumed to be either solar or five times solar. Two alternative input continua were used: 1) the standard AGN continuum of CLOUDY which is equivalent to the continuum described by Mathews and Ferland (1987) and 2) the low-*z* quasar continuum of Laor et al. (1997a). Computed line ratios are almost identical for fixed (U, n_e). However the ionizing luminosity differs by more than a factor of 2 for a fixed specific continuum luminosity. The contour plots showing the distributions of Al^{III}λ1860/ Si^{III}]λ1892,

$\text{SiII}\lambda 1814 / \text{SiII}\lambda 1892$, $\text{CIV}\lambda 1549 / \text{SiII}\lambda 1892$, and $\text{CIII}\lambda 1909 / \text{SiII}\lambda 1892$ (Fig. 9) are generated from $29 \times 19 = 551$ simulations and assume a standard set of simulations using a Mathews and Ferland (1987) continuum, $N_e = 10^{23} \text{ cm}^{-2}$, and solar metallicity. The CLOUDY 08.00 computations included a model of the Fe^+ ion with 371 levels. The UV FeII template, described in §4.2 is based on a suitable CLOUDY simulation. Even if a relationship is very likely between the dense low ionization gas producing our diagnostic lines and FeII emission (supported observationally) our diagnostics do not use any FeII computation. The weak line $\text{OI}\lambda 1304$ is used only for rest frame estimation and not for diagnostic considerations.

Apart from the hypothesis of plane-parallel geometry, no inferences are made about the actual distribution, location, and kinematics of the line emitting gas. The assumption of constant density is crude. If gas is distributed in clouds then magnetic confinement appears to be unnecessary to avoid cloud dispersion from pressure imbalance or cloud shear associated with a hot confining medium. Magnetic confinement could make density uniform within the cloud (Rees 1987; Bottorff and Ferland 2000).

6.2. Intermediate Ionization Lines in the Blend at $\lambda 1900$

The ratio $\text{CIII}\lambda 1909 / \text{SiII}\lambda 1892$ is density dependent because the transition probabilities of the two lines are so different: 114 s^{-1} vs 12600 s^{-1} (see Table 1. The forbidden lines at 1883\AA and 1907\AA have such low transition probabilities that they are collisionally quenched at much lower density and will not be considered. Line ratios like $\text{CIII}\lambda 1909 / \text{SiII}\lambda 1892$ are useful diagnostics in a rather narrow range of

density which depends on the transition probabilities. Above the critical density, emission lines originating from forbidden or semi-forbidden transitions become collisionally quenched, and hence weaker than lines for which collisional effects are still negligible. CIII] λ 1909 is clearly unsuitable as a diagnostic for $n_e \gtrsim 10^{11} \text{ cm}^{-3}$, as the CIII] λ 1909/ SiIII] λ 1892 $\rightarrow 0$. Feldman et al. (1992) gives critical density of SiIII] λ 1892 $n_e \sim 2 \cdot 10^{11} \text{ cm}^{-3}$. AlIII] λ 1860 is a permitted transition with large transition probability ($A \sim 5 \cdot 10^8 \text{ s}^{-1}$) and has no well-defined critical density (i.e., its equivalent width goes to zero toward thermodynamic equilibrium, which occurs at very high density, when all line emission is collisionally quenched). Our 2D array of CLOUDY simulations shows that the ratio AlIII] λ 1860/ SiIII] λ 1892 is well suited to sample the density range $10^{10} - 10^{12.5} \text{ cm}^{-3}$. Within this range the SiIII] λ 1892 intensity decreases smoothly by a factor 10; above the upper limit in density, the predicted intensity of SiIII] λ 1892 decreases. This corresponds to the densest, low ionization emitting regions likely associated to the production of FeII.

Intermediate-ionization lines such as CIII] λ 1909, AlIII] λ 1860, SiIII] λ 1892 avoid the problem of collisional ionization since the ionization potentials are rather high. The widely separated doublet AlIII] λ 1860 is expected to be produced entirely in the high-ionization zone (Laor et al. 1997b). CLOUDY simulations confirm this suggestion. Figure 10 (upper panel) shows the ionic fraction as a function of the geometrical depth in a cloud (or slab) of fixed column density ($N_c = 10^{23} \text{ cm}^{-2}$) and density ($n_e = 10^{12.5} \text{ cm}^{-3}$). As it can be seen, Al⁺⁺, Fe⁺⁺, and Si⁺⁺ share a region of dominance deep in the cloud, close to the end of the Strömgren sphere. Beyond, in the partially-ionized zone (PIZ) there is, as by definition, a significant fraction of ionized hydrogen. The dominant ionic stages of Si and Fe become Fe⁺

and Si^+ . It is very appropriate to consider the $\text{AlIII}\lambda 1860 / \text{SiIII}\lambda 1892$ ratio since the two lines are apparently emitted in the very same zones within the gas slab. Available reverberation mapping results may support this interpretation but are rather difficult to extrapolate since they are limited to $\text{CIII}\lambda 1909$ and to just one object (NGC 5548). The main finding is that $\text{CIII}\lambda 1909$ responds to continuum changes as $\text{H}\beta$ does (Peterson et al. 2004). Since response time generally depends on the ionization potential, we expect $\text{SiIII}\lambda 1892$ and $\text{AlIII}\lambda 1860$ to show a similar behavior. The Si^+ ionization potential is lower than that of C^+ ; the Al^+ ionization potential is slightly larger but comparable and still well below the one of HILs, $X^{i-1} \gtrsim 50$ eV.

6.3. The SiIII Contribution to the UV Spectrum of Quasars

AGN have a rather rich singly-ionized silicon spectrum in the range 1000-2000 Å, due to several resonant transitions from the ground term $3s^23p^12P^0$ to terms associated to the $3s^13p^2$ ($\lambda 1814$ and $\lambda 1304$), $3s^24s$ ($\lambda 1531$), $3s^23d$ ($\lambda 1263$) electronic configurations. A feature on the red side of $\text{Ly}\alpha$, at 1263 Å is detected in several Pop. A sources like I Zw 1 (Marziani et al. 2010).

The $\lambda 1309$ feature is partially blended with the OI triplet associated with a Bowen fluorescence mechanism from $\text{HI Ly}\beta$. The $\lambda 1309$ line is well resolved in sources like I Zw 1 with the extension of the broad $\lambda 1309$ feature suggesting significant SiIII emission around $\lambda 1309$. The $\lambda 1531$ feature is blended with $\text{CIV}\lambda 1549$. High S/N spectra of low redshift sources from HST (Laor et al. 1994) as well as for quasars at $z \approx 4$ (Constantin et al. 2002) indicate that the feature is very weak in

most sources.

The SiII feature at $\lambda 1814$ is detected in at least four of the five quasars studied by Laor et al. (1994). In the 6 objects used for the E1 sequence of Marziani et al. (2010), it is detected without reasonable doubt in I Zw 1 only. However this has to do more with the poor S/N of the 1900 Å region than of anything else; good S/N HST spectra show an unambiguous detection in Akn 120 and Mark 509, for example. Early detection of the UV SiII lines from IUE observations suggested collisional excitation and no relevant fluorescence effects (as observed in type Ia supernovæ; Dumont and Mathez 1981). Fluorescence effects and recombination are revealed by optical lines which are emitted through several cascade routes to the ground state. However, a median spectrum of A2 quasars with $S/N \approx 200$ (Zamfir et al. 2010) barely detects any expected emission feature in the range 4000-6500 Å. The prominence of the $\lambda 1814$ feature may then be associated to the relatively low temperature believed to exist in the innermost part of the line emitting “cloud”, $T_e \sim 5000 - 8000^\circ$ K. We may consider the equivalent width (W) ratio between the doublet lines at 1264 and at 1816 Å both due to a $^2D_{\frac{5}{2}} \rightarrow ^2P_{\frac{3}{2}}$ transition; in the simplest case we have: $W_{1263}/W_{1814} \approx (N_{u,1264}/N_{u,1816}) (f_{1264}/f_{1816}) (\lambda_{1264}/\lambda_{1816})^2 \approx 0.485 \frac{f_{1264}}{f_{1816}} e^{-\frac{\Delta E}{kT}} \approx 0.27$ if $T = 5000^\circ$, where f is the oscillator strength, and the energy difference between the transitions is $\Delta E \approx 3$ eV.

6.4. Use of the SiII λ 1814 and CIV λ 1549

The same caveats mentioned for the ratio CIII] λ 1909/ SiIII] λ 1892 apply to the AlIII λ 1860/ SiIII] λ 1892 ratio as well. The ground term 1S_0 has energy 16 eV and 24 eV for Si $^{+2}$ and C $^{+2}$ respectively. A dependence on the ionization parameter is expected, as already mentioned. However, given the similarity in the ionization structure of the photo-ionized slab, it is after all not surprising that the ratio AlIII λ 1860/ SiIII] λ 1892 is almost insensitive to the ionization parameter over a wide range of density. We remind that the detection of strong AlIII λ 1860 *alone* already suggests that we are considering very high density emitting gas even if metallicity is super-solar. Simulations indicate that AlIII λ 1860 should increase smoothly with density and be weakest in canonical BLR if the density is $n_e \sim 10^9 \text{ cm}^{-3}$ (cf. Korista et al. 1997). The ratio AlIII λ 1860/ SiIII] λ 1892 is therefore diagnosing high density gas, while the CIII] λ 1909/ SiIII] λ 1892 ratio covers the domain of $n_e \sim 10^{10} \text{ cm}^{-3}$. The ratio AlIII λ 1860/ SiIII] λ 1892 alone is, generally speaking, insufficient to determine n_e . A second diagnostic ratio is needed to constrain U and to unambiguously derive n_e . We consider both SiII λ 1814/ SiIII] λ 1892 and CIV λ 1549/ SiIII] λ 1892 as two diagnostic ratios suitable for constraining U , under the caveats described earlier.

The SiII λ 1814 doublet is conveniently placed, although weak or undetectable in most sources. The SiII λ 1814/ SiIII] λ 1892 ratio is anti-correlated with U in a regular form, as our CLOUDY simulations show, especially for $\log U \lesssim -2$, and for density not much above the critical density of SiIII] λ 1892. The behavior of the ratio SiII λ 1814/ SiIII] λ 1892 resembles the distribution of CIII] λ 1909/CIV λ 1549 in the plane (n_e, U) which shows a very regular dependence and a smooth anti-correlation

with U until the collisional quenching of $\text{CIII}\lambda 1909$ sets on. However, the IP of Si^0 is just 8 eV. The $\lambda 1814$ doublet is emitted in the partially ionized zone. Fig 10 (lower panel) shows the behavior of the volume emissivity ϵ times the geometrical depth within an emitting slab of gas as a function of the depth itself. Since the actual line emission is proportional to $\epsilon \cdot h$ reported in Fig. 10, the emission of the $\text{AlIII}\lambda 1860$, and $\text{SiIII}\lambda 1892$ lines is negligible in the PIZ, but the one of $\text{H}\beta$ certainly is not, and may be well dominating if $N_c \gg 10^{23} \text{cm}^{-2}$. Significant emission in the PIZ is expected also for the $\text{SiII}\lambda 1814$ doublet. However, for this latter line, total emission should not depend strongly on column density, since the emissivity becomes very low at $N_c \gtrsim 10^{23} \text{cm}^{-2}$. We note in passing that the $\text{H}\beta$ emissivity distributions advises against the inclusion of $\text{H}\beta$ (and other Balmer lines as well) in any diagnostics: due to strong line emission in the PIZ, any result is strongly dependent on N_c (Popović et al. 2008). If higher N_c are considered (up to 10^{25}cm^{-2}), ratios including $\text{SiIII}\lambda 1892$, $\text{AlIII}\lambda 1860$, and $\text{SiII}\lambda 1814$ show a very weak dependence on column density, with changes a few percent at worst.

We attempted to isolate a $\text{CIV}\lambda 1549$ component that corresponds to the $\text{AlIII}\lambda 1860$ and $\text{SiIII}\lambda 1892$ lines. This can be a small part of the total $\text{CIV}\lambda 1549$ emission, but there is no point to consider the whole $\text{CIV}\lambda 1549$ emission when $\text{CIV}\lambda 1549$ shows a large blueshift and is much broader than $\text{H}\beta$ (Fig. 5 of Sulentic et al. 2000) and $\text{SiIII}\lambda 1892$ and $\text{AlIII}\lambda 1860$ (Fig. 2 of Marziani et al. 2010). Taking into account various sources of ambiguity (mainly uncertainty in the quasar rest frame, S/N, blending with $\text{HeII}\lambda 1640$), the $\text{CIV}\lambda 1549$ BC component is constrained within $\pm 50\%$ at worst. We expect significant $\text{CIV}\lambda 1549$ emission from the low-ionization gas, and the basic assumption is that its $\text{CIV}\lambda 1549$ profile is the

same of the $\text{AlIII}\lambda 1860$, $\text{SiIII}]\lambda 1892$ lines. If one considers the emissivity behavior, $\text{CIV}\lambda 1549$ is obviously favored within the HIZ and almost constant until the end of the He^{++} zone is reached. The total emission increases with ionization parameter in a way that is roughly independent on density (all other parameters remaining fixed). The previous considerations are helpful to understand why the $\text{CIV}\lambda 1549$ ratios provide clear diagnostics of the ionization parameter and seem to be in very good with ratios employing lower ionization lines like $\text{SiII}\lambda 1814 / \text{SiIII}]\lambda 1892$ that is also mainly sensitive to U . The striking fact that the $\text{CIV}\lambda 1549$ emission confirms low-ionization supports the hypothesis that the three lines are emitted by the same region.

We note that the diagnostic ratio converge to regions that are *not* the region of maximum emission in the $U-n_e$ parameter space (cf. Baldwin, Ferland, Korista, & Verner 1995), although significant emission is always expected in any line we consider (i.e., no diagnostic ratio is build on lines of negligible emission with respect to the maximum emission in the $U-n_e$ parameter space).

7. Results on two Extreme, Elucidating Cases

We analyze two extreme objects – one extreme Pop. A and one extreme Pop. B – with the same methodology we used previously. The aim of this analysis is to help the interpretation of the line components measured on the spectra of the 8 $z \approx 3$ quasars.

7.1. SDSS Weak CIII] λ 1909 source: SDSS J120144.36+011611.6

Our project stems from the careful analysis of the I Zw 1 UV spectrum by Laor et al. (1997b), and the evidence of a well-defined trend in the λ 1900Å blend along the E1 sequence (Bachev et al. 2004, and Marziani et al., 2010). The NLSy1 I Zw 1 is known to be a sort of extremum in the E1 sequence: it shows strong FeII and FeIII, prominent AlIII λ 1860 and SiIII] λ 1892 emission. It is a representative example of the A3 spectral type, whose median 1900Å blend is shown in Fig. 3 of Bachev et al. (2004). Definitely, these sources are present also at intermediate to high redshift. We describe here the analysis of one source, SDSS J120144.36+011611.6 (Fig. 8), which seems to be a high-redshift, high-luminosity replica of I Zw 1, with broader lines (the FWHM limit of NLSy1s and Pop. A sources is luminosity dependent; see Netzer & Tahktenbrot 2007 and Marziani et al. 2009). These sources are Pop. A, and we assume that the profile of the BC is Lorentzian. Hereafter unshifted Lorentzian part of the line is said to be BC. Pop. A sources are also free of any VBC, making the analysis of the blend simpler.

Several considerations can be made from Fig. 8.

AlIII λ 1860 The lines less ambiguous to measure are the AlIII λ 1860 doublet because the two lines are less blended with other features, and they are remarkably strong. SiIII] λ 1892 is more heavily blended with CIII] λ 1909 and FeIII. However, the SPECFIT routine allows usually a plausible deconvolution of SiIII] λ 1892, making the AlIII λ 1860/ SiIII] λ 1892 ratio very reliable. FeII and FeIII are obviously strong. We can use FeII UV 191 to set roughly the level of FeII, while the feature at 2080Å

is helpful to estimate intensity of FeIII.

FeIII Our specfit analysis produces a very weak CIII]λ1909 component. A precise measurement of CIII]λ1909 is cumbersome, since its intensity depends on the actual FeIII emission. The strong feature at λ1914 could be dominating, and the template may seriously underestimate it (see Vestergaard and Wilkes 2001 for several alternatives in the empirical FeIII emission of I Zw 1). In any case the residual CIII]λ1909 emission is small, suggesting that the λ1900 blend, once believed to be mostly CIII]λ1909, is actually almost void of CIII]λ1909 emission in these A3-type sources.

SiIIλ1814 The SiIIλ1814 line is well visible in the spectrum of SDSS J120144.36+011611.6 and can be used as a substitute of CIVλ1549 to measure the ionization parameter. The ratio SiIIλ1814/ SiIII]λ1892 is mainly sensitive to the ionization parameters, as it is the ratio CIVλ1549/ SiIII]λ1892. The ratio SiIIλ1814/ SiIII]λ1892 has the considerable advantage of being weakly dependent on metallicity. If metallicity is known (see also §8.1), the ratio CIVλ1549/AlIIIλ1860 should be in principle preferred since AlIIIλ1860 is emitted through a permitted resonance transition while SiIIλ1814 is emitted in the collisionally excited, partially-ionized zone (PIZ).

CIVλ1549 - We fit CIVλ1549 with a Lorentzian component that is unshifted + a CIVλ1549 BBC. Note that the lack of shift in AlIIIλ1860 and SiIII]λ1892 imposes a strong, determinant condition on the strength of the Lorentzian-component in

CIV λ 1549. It is important to stress that some CIV λ 1549 BC emission is expected to be present according to our array of simulations. The ratio CIV λ 1549/AlIII λ 1860 is rather modest, as we can easily see even by eye. We note in passing that the width of BCC is $\approx 10000 \text{ km s}^{-1}$, with a peak blueshift indicatively of -6000 km s^{-1} , significantly larger than the one measured on the CIV λ 1549 of I Zw 1 by Marziani et al. (2009).

We consider the measured line ratios in the plane U vs. n_e , and see where they cross. We find very high density and low ionization (Fig. 13).

7.1.1. Along the E1 Sequence: A More Complex Scenario

Looking at the fit solution (Fig. 8(1b)), it seems that our spectrum has almost no CIII] λ 1909. In many ways this is not surprising. The physical solutions in the (U, n_e) plane of Fig. 13, points toward very low ionization ($U \sim 10^{-3} - 10^{-2}$) and high density ($n_e \gtrsim 10^{12} \text{ cm}^{-3}$). At such high values of n_e we expect that CIII] λ 1909 is collisionally quenched, and no significant emission. The ratio CIII] λ 1909/CIV λ 1549 is expected to be just $\sim 10^{-2}$ in the dense LIL-BLR. Therefore we can say that sources like SDSS and I Zw 1 are extreme because all of the $\lambda 1900 \text{ \AA}$ blend is emitted by very low ionization, dense gas.

However, as soon as we move away from spectral types A3+ along the E1 sequence, we see that the prominence of AlIII λ 1860 diminishes greatly. The emission disappears altogether at the other end of the E1 sequence, where several lobe-dominated radio-loud sources are found. For most quasars we see that

CIII] λ 1909 is rather strong and unmistakably present. At a first glance this complicates the interpretation of the spectrum. However, one has to consider that CIII] λ 1909 can be emitted only by gas of much lower n_e than that of the region where the bulk of SiIII] λ 1892 and AlIII] λ 1860 is emitted. Our simulations show that AlIII] λ 1860 intensity grows smoothly as a function of density in the ionization parameter range of interest $-3 \lesssim \log U \lesssim -1$. This said, and considered the smooth trend we see from A3 to B1⁺, the most reasonable conclusion is that a dense region emits significantly whenever AlIII] λ 1860 emission is detected, although the relative prominence of the dense BC changes along the E1 sequence: it accounts for the entire LIL emission *only* in the most extreme Pop. A sources. The sequence of Fig. 3 of Bachev et al. (2004) seems to be mainly a sequence of prominence of AlIII] λ 1860+ SiIII] λ 1892 vs CIII] λ 1909.

So, a very important conclusion is that a very dense, low-ionization region exists in the wide majority of quasars. It is associated with FeII prominence, as such gas is expected to emit a strong low-ionization spectrum. The most extreme FeII emitters are also the most extreme AlIII] λ 1860 emitters; in some cases where no AlIII] λ 1860 emission is measured, we also fail to detect any FeII emission (Marziani et al. 2010). Where is this region located? Why there are such distinctive line profiles as Lorentzian? The second issue goes beyond the present paper; for the moment our aim is to measure line components of AlIII] λ 1860, SiII] λ 1814, SiIII] λ 1892 and CIV] λ 1549 that come from this region and to estimate its distance from the central black hole (§9).

7.2. The Other E1 Extremum: 3C 390.3

3C 390.3 is a lobe-dominated (LD) RL source, with very broad emission lines and no optical FeII within detection limits (see Marziani et al. 2003, for the criterion used). It also shows a large peak shift in its $H\beta$ profile, and prominent narrow lines ($[OIII]\lambda 5007$, $H\beta$), but also narrow components of $CIV\lambda 1549$ and $CIII]\lambda 1909$ which are all well separated from the broad $H\beta$ profile.

To deconvolve the blends around $CIII]\lambda 1909$ and $CIV\lambda 1549$, we assume that in these objects, we have the same emission line profiles as for $H\beta$. The $H\beta$ broad profile can be described as the sum of a BC and a VBC. An unusual property of the BC is its large peak blueshift (it is unusual because of the shift amplitude: even if median spectra of Pop. B sources show a small BC redshift, there is a pretty large scatter with both red- and blueshifted peaks observed in individual sources; Zamfir et al. 2010). Applying in a self consistent way the BC and VBC to the $CIII]\lambda 1909$ and $CIV\lambda 1549$ blends, leads to very interesting results as shown in Figure 8:

- $AlIII\lambda 1860$ is very weak or even absent;
- the $CIV\lambda 1549$ profile is very similar to the one of $H\beta$: BC+VBC accounts for more than 90% emission, with a possible, very weak contribution of the blueshifted component which is usually dominating in Pop. A sources;
- the red wing observed in the 1900\AA blend is accounted for only if there is a strong $CIII]\lambda 1909$ VBC, FeII and FeIII emission being below the detectability limit in this source;

- there is no evidence of a VBC in AlIII λ 1860 and SiIII] λ 1892.
- the ratio CIV λ 1549/CIII] λ 1909 BC is ≈ 10 , a far cry from the ratios observed in extreme Pop. A sources like I Zw 1 and SDSS J120144.36+011611.6;
- even more interesting we find a CIV λ 1549/CIII] λ 1909 VBC ≈ 10 , as for the BC.

We conclude that this object is fundamentally different from Pop. A sources. The low ionization, high density BC seems to be absent. The similarity in the CIV λ 1549/CIII] λ 1909 ratios suggest that we are observing a VBC only. We predict that FeII will remain undetected or found to be weak even with $S/N \rightarrow \infty$.

In the plane (U, n_e) of Figure 13, the line ratios converge to a point at $\log U \approx -1.5$, and $\log n_e \approx 10.1$ (the SiII λ 1814 line cannot be measured accurately since S/N is poor). In this case, the CIII] λ 1909/CIV λ 1549 ratio also converges toward a (U, n_e) value consistent with the one indicated by the AlIII λ 1860/SiII λ 1814. In most other cases, this does not happen because the AlIII λ 1860 doublet is too strong to be accounted for by gas of $n_e \sim 10^{10} \text{cm}^{-3}$ even at super-solar metallicity. Emission occurs at pretty high ionization, in conditions that once upon a time were thought to be standard in quasars (Davidson and Netzer 1979). This Pop. A and B difference at the extrema was already pointed out, in a semi-quantitative way, by Sulentic et al. (2000) and Marziani et al. (2001).

It is however important not to generalize the case of 3C 390.3 to the remaining Pop. B sources. In most of them, AlIII λ 1860 is detected, and there is evidence of strong CIII] λ 1909. Actually CIII] λ 1909 emission seems to be prominent in all

of our VLT quasars. This means that we are in a composite situation, where low-ionization, high-density emission is present, along with significant VBC and other emission. The two extreme cases help us however to understand these more complex cases.

8. Results on the $z \approx 3$ Quasars

To estimate $\log n_e$ and $\log U$ values, we use the CLOUDY contour plots of the ratios $\text{AlIII}\lambda 1860 / \text{SiIII}\lambda 1892$, $\text{SiII}\lambda 1814 / \text{SiIII}\lambda 1892$, $\text{CIV}\lambda 1549 / \text{SiIII}\lambda 1892$ and $\text{CIII}\lambda 1909 / \text{SiIII}\lambda 1892$ showed in Fig. 9¹. The data points of our objects are in regions where the ratios are well-defined. The ratios $\text{CIV}\lambda 1549 / \text{SiIII}\lambda 1892$ and $\text{SiII}\lambda 1814 / \text{SiIII}\lambda 1892$ are mainly sensitive to the ionization parameter U , while $\text{AlIII}\lambda 1860 / \text{SiIII}\lambda 1892$ and $\text{CIII}\lambda 1909 / \text{SiIII}\lambda 1892$ are mainly sensitive to the electron density. We know that $\text{CIII}\lambda 1909$ is collisionally quenched at $\log n_e \gtrsim 10$ and in the contour plot for $\text{CIII}\lambda 1909 / \text{SiIII}\lambda 1892$ we see a step around this value.

We measure the BC intensity of $\text{SiIII}\lambda 1892$, $\text{AlIII}\lambda 1860$, $\text{SiII}\lambda 1814$ and $\text{CIV}\lambda 1549$; with them we compute the diagnostic ratios (for 3C390.3 we use $\text{CIII}\lambda 1909$ in place of $\text{SiII}\lambda 1814$; however there is no object similar to 3C390.3 among the $z \approx 2$ quasars). We present the fluxes of the line components in Tab. 3 and the equivalent width in Tab. 4. For the $\text{CIII}\lambda 1909$ line we show values only for

¹Note that there are regions where the ratio values are actually undefined: close to the high U limit ($\log U \gtrsim -0.3$), ratios $\text{AlIII}\lambda 1860 / \text{SiIII}\lambda 1892$ and $\text{SiII}\lambda 1814 / \text{SiIII}\lambda 1892$ (with $n_e \lesssim 10^9 \text{cm}^{-3}$) should not be considered.

Pop. B objects; we do not report $\text{CIII}\lambda 1909$ for Pop. A or boundary Pop. A to B objects because FeIII contamination is uncertain. For $\text{CIV}\lambda 1549$ line we also show the blue shifted and the very broad components, and in the last column we present the total flux of $\text{CIV}\lambda 1549$. Errors are at a 2σ confidence level, and include the sources of uncertainty described in §4.4. Errors are then quadratically propagated according to standard practice to compute intensity ratios and their logarithm.

Table 5 reports the diagnostic ratios actually used. For the BAL quasar J02287+0002 we present the values for both fits. For the extreme object 3C390.3 we use the ratio $\text{CIII}\lambda 1909 / \text{SiIII}\lambda 1892$. As we see in Fig. 1, $\text{SiII}\lambda 1814$ is absorbed by telluric B band in the objects J00103-0037, J03036-0023, J20497-0554 (most affected). We will not consider $\text{SiII}\lambda 1814$ to compute n_e and U on those cases. However, if we take at face value the $\text{SiII}\lambda 1814$ measure, it will converge close to the point set by the remaining two ratios. We display on a graph a line representing the behavior of each ratio; the ideal point where the lines representing different diagnostic ratios cross determines the values of $\log n_e$ and $\log U$. Figs. 11 and 12 shows the contour plots where we can see that the diagnostic ratios converge to rather well defined values. The cross point is very precise for the objects J00103-0037, J00521-1108 and J02287+0002; for the remaining objects J01225+1339, J02390-0038, J03036-0023, J20497-0554 and J23509-0052 the cross point is slightly different. We must not forget the errors involving the fits, such as the changing of the shape profile that makes large the peak intensity if is Lorentzian or it could be less intense if it is Gaussian; the FeII pseudo-continuum contribution that affects principally to $\text{SiII}\lambda 1814$ or the FeIII that in some cases affects to $\text{SiIII}\lambda 1892$. As we will show later, significant disagreement above the measurement

errors indicates supersolar metallicity (§8.1)

For the objects J00103-0037, J03036-0023 and J20497-0554 we exclude the SiII λ 1814 line from the diagnostic ratios because it is affected by absorption. For the remaining objects, we take the average of the crossing contour plots of $\text{Log}(\text{AlIII}\lambda 1860 / \text{SiIII}\lambda 1892)$ crossing with $\text{Log}(\text{CIV}\lambda 1549 / \text{SiIII}\lambda 1892)$ and $\text{Log}(\text{AlIII}\lambda 1860 / \text{SiIII}\lambda 1892)$ crossing with $\text{Log}(\text{SiII}\lambda 1814 / \text{SiIII}\lambda 1892)$. For 3C390.3 we use $\text{Log}(\text{CIII}\lambda 1909 / \text{SiIII}\lambda 1892)$ instead of $\text{Log}(\text{SiII}\lambda 1814 / \text{SiIII}\lambda 1892)$. Table 6 summarizes the $\log n_e$ and $\log U$ values including their uncertainty. Since U and n_e are not independent quantities (their correlation coefficient is found to be 0.55), we adopt the appropriate formula for the errors on the product Un_e (following Bevington 1969). We present average values for extreme objects of the crossing points of figures 13 and 14(e). In the SDSS J12014+0116 case we give full weight to the SiII λ 1814 measurement. The crossing points disagree somewhat for SDSS J12014+0116. This could be due to an underestimate of *both* SiII λ 1814 and CIV λ 1549 in the fits. On the one hand, SiII λ 1814 is clearly seen and strong but is contaminated by FeII blend; on the other hand, CIV λ 1549 is strongly affected by the blue-shifted component and by the assumption that it is of Gaussian shape. An increase by 30% in the measurement of the intensity of the two line would lead to a better agreement. At any rate, the convergence is toward a value of $\log U \approx -3$, lower than for the other $z \approx 3$ quasars. This is reflected in the CIV λ 1549 EW of this source, also significantly lower.

Table 7 reports the results of the fits of our 8 objects and in the last 3 rows the average values of the extreme objects. Column 1 identifies the quasar; Col. 2 gives

the proper distance in cm; Cols. 3 and 4 are the continuum specific flux value at 1350\AA and 1700\AA respectively, Col. 5 reports the FWHM in km s^{-1} for the broad components, Col. 6 is the Population designation. The objects J01225+1339 and J23509-0052 are at the boundary between Pop. A and B because because FWHM is near to 4000 km s^{-1} (see §1.2). Col. 7 provides the product $n_e \cdot U$ of table 6. Column 8 shows the the average of the logarithm of the size of the BLR in cm using the Spectral Energy Distribution (SED) of Laor et al. (1997a) and the one of Mathews and Ferland (1987) shown in Fig. 15. Column 9 is the average of the logarithm of the black hole mass in solar masses using both SED. The difference in r_{BLR} and M_{BH} computed with the two SEDs is constant and equal to ≈ 0.17 dex. Finally Col. 10 is black hole mass in solar masses computed from Vestergaard and Peterson (2006) formula (Equation 11). We will explain the next section how these quantities are computed.

8.1. Effects of Metallicity

The lines employed in the present study come from carbon, silicon and aluminium; all these element can be significantly depleted from gas if dust grains are formed (e. g., Mathis 1990). However, the emitting regions where our lines are produced are thought too hot to contain significant amount of dust (a definition of broad line region is right the central engine region below the dust sublimation region: e.g., Elitzur 2009). In addition Si and Al are expected to be produced in similar circumstances in the late stage of evolution of massive stars (Clayton 1983, Ch. 7). We note also that the $\text{CIV}\lambda 1549 / \text{SiIII}\lambda 1892$ and $\text{CIV}\lambda 1549 / \text{AlIII}\lambda 1860$

usually results that are in perfect agreement in the plane (n_e, U) . These findings support our assumption that, if metallicity variations are present, the relative abundance $[\text{Al}:\text{Si}]$ remains constant. We assume that also $[\text{Al}:\text{Si}:\text{C}]$ is constant.

The strength of $\text{NV}\lambda 1240$ relative to $\text{CIV}\lambda 1549$ and $\text{HeII}\lambda 1640$ suggest supersolar chemical abundances (Hamann and Ferland 1993; Hamann & Ferland 1999). Chemical abundances may be well 5 to 10 times solar (Dhanda et al. 2007), with $Z \approx 5Z_\odot$ reputed typical of high z quasars (Ferland et al. 1996). An array of simulations as a function of ionization parameter was computed under for $Z = 5Z_\odot$. As expected, we find that the ratio $\text{AlIII}\lambda 1860 / \text{SiIII}\lambda 1892$ is not strongly dependent on Z : the ratio increases by about 40% passing from $Z = 1Z_\odot$ to $Z = 5Z_\odot$, for $\log n_e \approx 12$ and $\log U \approx -2$. The same is true for the $\text{SiIII}\lambda 1814 / \text{SiIII}\lambda 1892$ ratio. Since the first ratio sets n_e , and the second U , these two ratios should be preferred because they provide n_e and U values that are weakly affected by a factor 5 change in density. The effect is comparable to the other major sources of uncertainty discussed previously.

The E1 sequence seems to be mainly a sequence of ionization in the sense of a steady decrease in prominence of the low-ionization BC toward Population B (Marziani et al. 2001, 2010). However, this is not to neglect that metal-enrichment also plays a role, especially for the most extreme Pop. A sources i.e., those in bin A3 and higher (Sulentic et al. 2001). The two extreme cases seem to be revealing in this respect. All ratios converge to a well defined point in the case of 3C 390.3 (see Fig. 13, left panel). In this case there is no major evidence of supersolar metallicity. The converse is true in the case of SDSS J120144.36+011611.6. The

ratios involving $\text{CIV}\lambda 1549$ indicate a lower ionization level, with $U \log \sim -3$. This is because $\text{AlIII}\lambda 1860$ and $\text{SiIII}]\lambda 1892$ too strong with respect to $\text{CIV}\lambda 1549$. The $\text{CIV}\lambda 1549$ intensity depends weakly on Z while the $\text{AlIII}\lambda 1860$ and $\text{SiIII}]\lambda 1892$ lines are more sensitive. The $Z = 5Z_{\odot}$ yields values closer to the ones obtained from the Si and Al line ratios, but not yet in concordance. We suggest that this source could be of even higher metallicity, $Z \sim 10Z_{\odot}$.

In principle, the discrepancy in the intersection point, with $\text{SiIII}]\lambda 1892/\text{CIV}\lambda 1549$ and $\text{AlIII}\lambda 1860/\text{CIV}\lambda 1549$ yielding lower U than the Al-Si ratios, should signal a significant enrichment of the BLR gas. Appreciable discrepancy is visible in the contour plots of the BAL quasar J01225+1339, J03036-0023, J20497-0554 and J23509-0052 if $Z = Z_{\odot}$ is assumed. In the same plots made for $Z = 5Z_{\odot}$, the agreement becomes very good (see Fig. 14). High metallicity yields higher U and somewhat smaller n_e . In the case of two sources, J02390-0038 and J20497-0554, the discrepancy of the crossing lines might indicate $Z_{\odot} \lesssim Z \lesssim 5Z_{\odot}$. A coarse r_{BLR} and M_{BH} estimate can be obtained considering only the $\text{SiII}\lambda 1814/\text{SiIII}]\lambda 1892$ and $\text{AlIII}\lambda 1860/\text{SiIII}]\lambda 1892$ ratios.

We conclude that the effect of metallicity is between the uncertainty of the method if the ratios $\text{SiII}\lambda 1814/\text{SiIII}]\lambda 1892$ and $\text{AlIII}\lambda 1860/\text{SiIII}]\lambda 1892$ are considered to compute n_e and U . It is significant if the ratios containing $\text{CIV}\lambda 1549$ are included. The amplitude of the effect is about a factor 2 on the r_{BLR} and M_{BH} estimates in the case of SDSS J120144.36+011611.6, where highly supersolar metallicity is probably appropriate. A more refined approach could exploit the dependence of the $\text{AlIII}\lambda 1860/\text{CIV}\lambda 1549$ (and $\text{SiIII}]\lambda 1892/\text{CIV}\lambda 1549$) on Z to build

a 3D diagram where n_e , U , and Z can be determined independently.

9. A Photoionization Method to Compute the Broad Line Region Distance and the Black Hole Mass.

The distance of the broad line region (r_{BLR}) from the central continuum source the black hole mass (M_{BH}) are key parameters that let us understand the dynamics of the gas in the emitting region and the quasar behavior and evolution. In this work we will use a method based on the determination of n_e and U to compute r_{BLR} . Eq. 1 can be rewritten as

$$r_{BLR} = \left[\frac{\int_{\nu_0}^{+\infty} \frac{L_\nu}{h\nu} d\nu}{4\pi U n_e c} \right]^{1/2} \quad (2)$$

and also as

$$r_{BLR} = \frac{1}{h^{1/2} c} (U n_e)^{-1/2} \left(\int_0^{\lambda_{Ly}} f_\lambda \lambda d\lambda \right)^{1/2} d_p \quad (3)$$

where h is the plank constant, c is the light speed, d_p is the proper distance. The integral is carried out from the Lyman limit to the shortest wavelengths on the *rest frame* specific flux f_λ . For the integral we will use two Spectral Energy Distributions (SEDs): one described by Mathews & Ferland (1987) and one by Laor et al. (1997a), also reproduced in Fig. 15. The quasar distance d_p is computed from the redshift using the following approximation (Sulentic et al. 2006b), derived assuming $H_0 = 70 \text{ km s}^{-1} \text{ Mpc}^{-1}$ and a relative energy density $\Omega_\Lambda = 0.7$ and $\Omega_M = 0.3$:

$$d_P \approx \frac{c}{H_0} \left[1.500 \left(1 - e^{-\frac{z}{6.107}} \right) + 0.996 \left(1 - e^{-\frac{z}{1.266}} \right) \right]. \quad (4)$$

Knowing r_{BLR} we can calculate the M_{BH} assuming virial motions of the gas

$$M_{\text{BH}} = f \frac{\Delta v^2 r_{\text{BLR}}}{G}. \quad (5)$$

or,

$$M_{\text{BH}} = \frac{3}{4G} f_{0.75} (\text{FWHM})^2 r_{\text{BLR}} \quad (6)$$

with the geometry term $f \approx 1.4$, corresponding to $f_{0.75} \approx 1.9$ (Onken et al. 2004; see also Woo et al. 2010). Collin et al. (2006) suggest that f is significantly different for Pop.A and B sources; we do not consider here their important result for the sake of comparison with previous work (§10.2). The resulting r_{BLR} and M_{BH} are reported in Columns 8 and 9 of Table 7. Errors are at 2σ confidence level and have been computed propagating quadratically the major sources of uncertainty. More precisely, in addition to the error on $\log(n_e U)$, the r_{BLR} determination is affected by the uncertainty in the spectrophotometry (specific fluxes of Col. 3 of Tab. 7), and errors on the shape of the ionizing continuum. The two SEDs that we assumed as extreme yield a difference in ionizing photons of a factor 2.2. At a $2\text{-}\sigma$ confidence level this corresponds to an uncertainty of ± 0.065 in logarithm. An additional source of uncertainty affects M_{BH} due to the FWHM determination. Errors on FWHM are quadratically added to the uncertainty on r_{BLR} in the values reported as $\log M_{\text{BH}}$ errors.

10. Discussion

10.1. Previous work

There have been several studies aimed at computing r_{BLR} and M_{BH} . A direct measure of r_{BLR} through reverberation mapping requires an enormous amount of observational effort and has only been applied to a relatively small number of quasars: slightly less than 50 objects with $z \lesssim 0.4$ (Kaspi et al. 2000, 2005, Peterson et al. 2004; Bentz et al. 2010). A second way to measure r_{BLR} uses a less direct method. Kaspi et al. (2000, 2005) and Bentz et al. (2009) used reverberation mapping results to find, in an empirical way, a relationship between r_{BLR} and the optical continuum luminosity at 5100\AA ,

$$r_{\text{BLR}} \propto L^\alpha \quad (7)$$

with $\alpha \approx 0.69$. Vestergaard & Peterson (2006) obtained a similar result for the optical continuum luminosity with an $\alpha \approx 0.50$ and for the UV continuum at 1350\AA , $\alpha \approx 0.53$. These relationships have been used to compute the r_{BLR} not only for nearby objects, but also for high redshift objects. There are other works that use single epoch spectra and the continuum at 3000\AA , obtaining an $\alpha \approx 0.47$ (McLure & Jarvis 2002).

Once we know the r_{BLR} , we can calculate the M_{BH} assuming virial motions of the gas. We can rewrite Eq. 5 as

$$M_{\text{BH}} \propto f \frac{\text{FWHM}^2 L^\alpha}{G}. \quad (8)$$

$\text{H}\beta$ is a low ionization strong line whose FWHM has been widely used

to determine the M_{BH} for objects mainly up to $z \lesssim 0.9$; above this limit IR spectrometers and large telescopes are needed to cover the redshifted line. For distant objects ($z \sim 2$), an alternative is to use C $\text{IV}\lambda 1549$, a high ionization line emitted in the UV. However, this line should be used with caution because the line is often blueshifted. This means that at least part of this line is likely emitted in an outflow (Sulentic et al. 2007). Thus the estimation of M_{BH} using $\text{FWHM}(\text{CIV}\lambda 1549)$ tend to be systematically higher than those using $\text{FWHM}(\text{H}\beta)$, especially for objects of Population A.

10.2. Comparison with Vestergaard and Peterson (2006)

As described above, the relationship of Eq. 3 has an index of $\alpha \approx 0.53$ for the UV continuum at 1350\AA :

$$r_{\text{BLR}} \propto L(1350\text{\AA})^{0.53} \quad (9)$$

Vestergaard & Peterson (2006) used this relation to obtain the following formula that relates M_{BH} to the $\text{FWHM}(\text{CIV}\lambda 1549)$ and the continuum luminosity at 1350\AA

$$\log M_{\text{BH}}(\text{CIV}) = \log \left\{ \left[\frac{\text{FWHM}(\text{CIV})}{1000 \text{ km s}^{-1}} \right]^2 \left[\frac{\lambda L_{\lambda}(1350\text{\AA})}{10^{44} \text{ ergs s}^{-1}} \right]^{0.53} \right\} + (6.66 \pm 0.01). \quad (10)$$

In columns 9 and 10 of table 7 and in Fig. 16 we compare our M_{BH} results with those using Eq. 10. We do not apply corrections for radiation-pressure effects that are likely relevant especially for objects radiating at large Eddington ratio (Netzer 2009; Netzer & Marziani 2010). The difference between this computation and the one reported in Sulentic et al. (2007) is that in the latter work the blueshifted component was not separated from the broad component of C $\text{IV}\lambda 1549$. Larger

values of $\text{FWHM}(\text{CIV}\lambda 1549)$ yielded M_{BH} much larger than the ones derived from $\text{FWHM}(\text{H}\beta)$ in Pop. A objects which show large contributions of the blueshifted component.

We compare the masses obtained using our photoionization method with those of Vestergaard & Peterson (2006) in Fig. 16. From our results we can see that the masses match very well. This indicates that the Kaspi et al (2000) relationships can be extended to be used in high redshift objects (or at least until $z\sim 3$) if the FWHM of the core broad line region can be well determined and measured. In order to do this, we need:

- Spectra with S/N high enough to see the profile shape that allows decomposition of the $\text{CIV}\lambda 1549$ line, especially to separate the blue component from the broad core;
- to follow the methodological considerations explained in §4.

Fig. 16 should be looked at with two cautions. First, the correlation is dominated by the luminosity dependence of r_{BLR} , used to compute M_{BH} in both cases. Second, the spread of M_{BH} values is small, less than one order of magnitude (and most objects have statistically indistinguishable masses). Our estimated error bars are however small compared to the spread expected on the basis of the $r_{\text{BLR}}-L$ correlation which is, according to Vestergaard & Peterson (2006), ± 0.66 at a 2σ confidence level. The two shaded bands of Fig. 16 limit the region where we can expect to find data points on the basis of the $r_{\text{BLR}}-L$ correlation. Clearly, a proper interpretation of the $\text{CIV}\lambda 1549$ profile may help to reduce the scatter. In any case,

our estimate should provide better M_{BH} estimates.

10.3. The LIL-BLR

While the existence of high density and low ionization has been invoked since long to explain FeII emission (especially by S. Collin and collaborators, as mentioned in the introduction), we have provided additional evidence that high density and low ionization are indeed diagnosed from emission lines other than FeII blends, and that conditions are the one producing most line emission in extreme Pop. A quasars. Last but not least, both U and n_e can be observationally determined with reasonable accuracy from the diagnostic ratios SiII λ 1814/ SiIII λ 1892, AlIII λ 1860/ SiIII λ 1892, and CIV λ 1549/(AlIII λ 1860 or SiIII λ 1892). These ratios are pretty well defined, while estimating CIII λ 1909 and FeIII λ 1914 relative contribution is not relevant to our method (with the exceptions of the rare sources like 3C 390.3). This low ionization BLR (or LIL BLR) has very similar properties to the OI and CaII emitting region identified by Matsuoka et al. (2008). The LIL-BLR seems to be present in the vast majority of quasars, probably all the ones with significant FeII emission (Marziani et al. 2010). The low values of U could be a consequence of the high density rather than of a far away location of the emitting region. The assumption of a single well defined value of U and n_e is probably an idealization even for the LIL-BLR taken alone; however the convergence of emission line ratios toward a well defined point, along with the ability to qualitatively explain FeII and most H β emission, indicate that the LIL-BLR might be a region with a small range of low U and high n_e .

Do density and ionization parameter in the LIL BLR converge to a single well defined value with a small dispersion? A tentative answer comes from the values reported in Tab. 6. Excluding 3C390.3, the range U and n_e span is not very large (even considering changes in metallicity): less than one order of magnitude around $\log n_e \sim 12$, and ionization parameter $\sim -2 - 2.5$, and the spread is not much larger than the uncertainties in the individual measurements. The product $U \cdot n_e$ seems to be fairly stable. If we exclude J03036-0023 with the unusually low value of 8.96, we have $\langle \log(U \cdot n_e) \rangle \approx 9.55$, with a sample dispersion of 0.11. We applied the same method to 14 low- z quasars (Negrete et al. 2010), and we obtain $\langle \log(U \cdot n_e) \rangle \approx 9.7$, with a dispersion of 0.3. Assuming $\log(U \cdot n_e) \approx 9.6$ could be a good approach to estimate M_{BH} if elaborate measurements on C IV $\lambda 1549$ and C III] $\lambda 1909$ are not possible, and only a rough estimate of the Si III] $\lambda 1892$ FWHM is available. On the other hand, there is still a major effect of measurement errors on the uncertainty derived for $\log(U \cdot n_e)$; instrumental improvements may lead to a significant appreciation of object-by-object diversity.

The $U \cdot n_e$ values reported in Table 7 are not very far from the average value obtained by Padovani and Rafanelli (1988). This is not surprising since the spectra at low and high z seems to show the same diversity, classified through the E1 sequence and the Pop. A/Pop. B distinction. In other words, NLSy1-like sources whose spectrum is similar to I Zw1 appear to be present at high redshift, meaning that the LIL-BLR remains strong and prominent over a wide range of redshifts. A second reason is that Padovani and Rafanelli (1988) considered $\text{H}\beta$. Emission of $\text{H}\beta$ can be significant under a much wider range of U and n_e ; however, the Al III $\lambda 1860$, Mg II $\lambda 2800$, Fe II emitting region should be also a strong producer of $\text{H}\beta$. This region

with well-defined physical conditions is expected to be the emitter of the core of $H\beta$, i.e., the part of the line responding more strongly to continuum changes.

10.3.1. Verification on EW and Line Luminosity

Considering that we have very low ionization parameter values, a legitimate question is whether we have a sufficient number of photons to explain the EW and luminosity of the emission lines. We made a preliminary check of consistency for the EW from CLOUDY simulations. A second, a-posteriori test was to consider the predicted line luminosity assuming the actual luminosity of the quasar, the density and the distance r_{BLR} derived from our method, and spherical geometry.

A remarkable property common to all spectra is the low EW of the emission lines. The extreme source SDSS J120144.36+011611.6 has total $W(\text{CIV}\lambda 1549) \approx 19 \text{ \AA}$, which becomes $\approx 7 \text{ \AA}$ if only the LIL component is considered. The whole 1900 \AA blend has $W \approx 20 \text{ \AA}$; the individual EWs of $\text{SiIII}]\lambda 1892$ and $\text{AlIII}\lambda 1860$ are just a few \AA . Similar considerations apply to the other high- z quasars, especially for Pop. A sources. In this case we have $W(\text{CIV}\lambda 1549) \approx 20 - 30 \text{ \AA}$, the equivalent width of the whole 1900 \AA $30 - 40 \text{ \AA}$ including the uncertain contribution of FeIII and $\text{CIII}]\lambda 1909$. This has the important implication that the ionization parameter cannot be very large. From our simulations, we deduce that the LIL-BLR $\log U$ is always $\lesssim -2.0$. On the other hand, toward the low U , high density limit emission lines tend to disappear altogether. The predicted EWs become too low to account for the observed EW with a covering factor $f_c \lesssim 0.5$ if $\log U \approx -3$. Cases of very low U are rather indicative of strong metal enhancement than of extremely low

ionization level (see §8.1). If we take $\log n_e \approx 12.5$, $\log U = -2.75$, the predicted equivalent width of is $W(\text{CIV}\lambda 1549) \approx 37 \text{ \AA}$ for a covering factor 0.5, close to the largest values observed in our quasars. However, The $\text{CIV}\lambda 1549$ EW of SDSS J12014+0116 can be accounted for by the values of $\log U \approx -3.00$ and $\log n_e \sim 12.75 - 12.50$.

If we model the BLR with a spherical geometry where the emitting gas covers a fraction f_c of the continuum, CLOUDY computations confirm that the line luminosity can be accounted for. The luminosity at 1700 \AA of J00103-0037 is $\log \lambda L_\lambda \approx 46.6$; the predicted luminosity of $\text{CIV}\lambda 1549$ is $\log L(\text{CIV}\lambda 1549) \approx 44.5$, under the assumption of $Z = Z_\odot$, $f_c = 0.1$, and Mathews & Ferland continuum shape. The observed $\text{CIV}\lambda 1549$ line luminosity of J00103-0037, $\approx 9 \cdot 10^{44} \text{ ergs s}^{-1}$, is obtained with $f_c \approx 0.3$.

10.4. Analogy with η Carinæ

The physical conditions we envisage for the BC of quasars find a correspondence in the so-called Weigelt blobs of η Carinæ, located in the equatorial plane of the system, perpendicular to the symmetry axis of the bipolar lobes forming the homunculus nebula (cf. Marziani et al. 2010). Unlike the gas of the bipolar lobes, predominantly shock heated, the Weigelt blobs are believed to be dense gas photoionized by the radiation associated to the central, massive star and to a possible companion (e.g., Johansson et al. 2000; Davidson 2005). The spectrum of the Weigelt blobs shows very weak $\text{CIII]}\lambda 1909$ along with a prominent line at $\lambda 1914$, ascribed to the $z^7P_3^0 \rightarrow a^7S_3$ FeIII transition. The line appears very

strong because the upper level is populated by Ly α fluorescence. This very same process is expected to be present also in quasars. Indeed, in I Zw 1, where lines are narrow, and in SDSS J120144.36+011611.6 the peak emission at around 1914 Å is actually visible. The amount of Ly α pumping cannot be estimated through the standard edition of CLOUDY (the Fe⁺² ion is not modeled). Additional photoionization computations including a suitable Fe⁺² model and line transfer should be considered. This is beyond the aim of the present study; we can conclude in a qualitative fashion that the spectrum of the η Carinae blobs supports a view of the low-ionization part of the BLR that is not conventional: very high density gas, at very low ionization.

11. Conclusions

In this paper we presented new observations of eight high redshift quasars. The spectra were meant to provide high S/N, moderate resolution data on which the CIV λ 1549, SiIII] λ 1892, AlIII λ 1860, and SiIII λ 1814 emission line profiles could be accurately analyzed. Line profile fits allowed us to isolate a specific component whose intensity ratios were used to derive consistent values for electron density and ionization parameter. This line component (LIL BC) seems to be emitted predominantly by low ionization, high density gas.

These results permitted us to compute the product $n_e \cdot U$ and hence the size of the Broad Line Region and the central black hole mass. The photoionization method outlines in this paper offers an estimate of r_{BLR} for each quasar, with some advantages on the r_{BLR} valued derived from the luminosity-size correlation.

The luminosity correlation suffers from large scatter and is simply extrapolated to very high luminosity without any support since there are, unfortunately, no conclusive results on reverberation of high luminosity quasars even if heroic efforts are underway (e.g., Trevese et al. 2007, Botti et al. 2010). We found that the black hole masses derived from the computed r_{BLR} and from the virial assumption are in good agreement with the ones derived from the luminosity-size relationship. Actually, Fig. 16 suggests that we reduced the errors of the M_{BH} by a factor of two with respect to the expectation from the Vestergaard & Peterson (2006) relationship.

We repeat that our M_{BH} and r_{BLR} results are based on the product $n_e \cdot U$ and not on values of n_e and of U taken separately. It seems that this product converges to two typical ranges of values, one of them associated to low-ionization, high density gas (the LIL-BLR). For our n_e and U determinations we do not use ratio $\text{CIII}] \lambda 1909 / \text{SiIII}] \lambda 1892$ except for 3C 390.3. As we discussed in §7.2, this ratio should not be considered at high density because $\text{CIII}] \lambda 1909$ is collisionally quenched if $n_e \gtrsim 10^{10} \text{ cm}^{-3}$. $\text{CIII}] \lambda 1909$ is produced in conditions that are very different from the ones we found for the LIL-BLR. While the method can be applied to most quasars, the application seems to be especially straightforward to quasars whose spectrum is like SDSS J120144.36+011611.6 (if high metallicity is properly taken into account) or, at the other end, 3C390.3. In the first case we have dominance by the LIL-BLR, in the second case the LIL-BLR seems to be completely absent and physical conditions look radically different: high ionization and moderate density. An inspection of SDSS spectra covering both the 1900 Å blend and $\text{CIV} \lambda 1549$ (up to $z \approx 3.5$) shows that SDSS J120144.36+011611.6 has many replicas at high

redshift, accounting for at least a few percent of all quasars. These high-metallicity objects should be the first candidates to expand black hole mass computations to high redshift without relying on the $r_{\text{BLR}} - L$ correlation.

To apply the photoionization method in the most effective way, determining n_e and U with the lowest uncertainty, spectral data should be of moderate resolution ($\lambda/\Delta\lambda \sim 1000$) as well as of high S/N. If the SiII λ 1814 line can be measured in an accurate way, it would be possible to derive independent estimates of U , n_e , and Z/Z_\odot in most quasars.

A. Negrete and D.Dultzin acknowledge support form grant IN111610 PAPIIT UNAM. Funding for the SDSS and SDSS-II has been provided by the Alfred P. Sloan Foundation, the Participating Institutions, the National Science Foundation, the U.S. Department of Energy, the National Aeronautics and Space Administration, the Japanese Monbukagakusho, the Max Planck Society, and the Higher Education Funding Council for England. The SDSS Web Site is <http://www.sdss.org>. The SDSS is managed by the Astrophysical Research Consortium for the Participating Institutions listed at the SDSS Web Site.

References

- Appenzeller, I., et al. 1998, The Messenger, 94, 1
- Bachev et al. 2004, ApJ, 617, 171
- Baldwin, Ferland, Korista and Verner, 1995, ApJ, 455, L119

- Baskin, A. & Laor, A. 2005, MNRAS, 356, 1029
- Bentz, M. C., et al. 2010, ApJ, 716, 993
- Bevington, P. R. 1969, Data reduction and error analysis for the physical sciences,
New York: McGraw-Hill, 1969
- Boroson, T.A. & Green, R.F., 1992, ApJS, 80, 109
- Botti, I., Lira, P., Netzer H., Kaspi, S. 2010, IAU Symposium, 267, 198
- Bottorff M.C. & Gary J.F. 2000, MNRAS, 316, 103
- Bruhweiler, F. & Verner, E., 2008, ApJ, 675, 83
- Clayton, D.D., 1983, Principles of Stellar Evolution & Nucleosynthesis,
Chicago:University of Chicago Press, Ch. 7
- Collin-Souffrin S. et al. 1988, MNRAS, 232, 539
- Collin, S., et al. 2006, A&A, 456, 75
- Constantin A. et al. 2002, ApJ, 565, 50
- Davidson, K. & Netzer, H., 1979, Rev. Mod. Phys. 51, 715
- Davidson, K. 2005, ASPC, 332, 101
- Dumont, A. M. & Mathez, G., 1981, A&A, 102, 1
- Dumont, A. M, & Collin-Souffrin, S., 1990 A&A 229, 292
- Edlén & Swings, 1942, ApJ, 95, 532
- Ekberg J.O. 1993, A&AS, 101, 1

- Espey, B. R., Carswell, R. F., Bailey, J. A., Smith, M. G., & Ward, M. J. 1989, ApJ, 342, 666
- Francis P.J. et al. 1991, ApJ, 373, 465
- Feibelman, W.A., and Aller, L.H., 1987, ApJ, 319, 407
- Feldman U. et al. 1992, ApJS, 81, 387
- Ferland G. J. et al. 1998, PASP, 110, 761
- Gaskell, C. M. 1982, ApJ, 263, 79
- Gaskell, M. et al. 1999, ASPC, 175, 423
- Hu, C., et al. 2008, ApJ, 687, 78
- Johansson S. et al. 2000, A&A, 361, 977
- Joly, M., 1987, A&A, 184,33
- Kaspi et al. 2000, ApJ, 533, 631
- Kaspi et al. 2005, ApJ, 629, 61
- Kriss G.A., 1994, ASPC, 61, 437
- Korista K. et al. 1997, ApJS, 108, 401
- Laor A. et al. 1994, ApJ, 420, 110
- Laor A. et al. 1997a, ApJ, 477, 93
- Laor A. et al. 1997b, ApJ, 489, 656

- McLure & Jarvis 2002, MNRAS, 337, 109
- Marziani, P., Sulentic, J. W., Dultzin-Hacyan, D., Calvani, M., & Moles, M. 1996, ApJS, 104, 37
- Marziani P. et al. 2003, ApJS, 145, 199
- Marziani P. et al. 2003b, MNRAS, 345, 1133
- Marziani P. et al. 2008, RMAA serie de conferencias, 32, 69
- Marziani P. et al. 2009, A&A, 495, 83
- Marziani P. et al. 2010, MNRAS, arXiv:1007.3187v1
- Matsuoka, Y., Kawara, K., & Oyabu, S. 2008, ApJ, 673, 62
- Mathews & Ferland 1987, ApJ, 323, 456
- Negrete, C. A., Dultzin, D., Marziani, P., Sulentic J. W. 2010, ApJL, submitted
- Netzer, H., & Trahtenbrot, B. 2007, ApJ, 654, 754
- Netzer, H. 2009, ApJ, 695, 793
- Netzer, H. & Marziani, P. 2010, ApJ, in press, arXiv:1006.3553v2
- Osterbrock, D. E., & Ferland, G. J. 2006, Astrophysics of gaseous nebulae and active galactic nuclei, 2nd. ed. by D.E. Osterbrock and G.J. Ferland. Sausalito, CA: University Science Books, 2006,
- Onken, C. A., Ferrarese, L., Merritt, D., Peterson, B. M., Pogge, R. W., Vestergaard, M., & Wandel, A. 2004, ApJ, 615, 645

- Padovani, P., 1988, A&A, 192, 9
- Padovani, P. & Rafanelli, P. 1988, A&A, 205, 53
- Padovani, P., Burg, R.I., Edelson, R.A., 1989, BAAS, 20, 969
- Peterson B. M. et al. 2004, ApJ, 613, 682.
- Popović L. et al. 2008, PASJ, 60, 1
- Rees M.J. 1987, MNRAS, 228, 47
- Richards, G. T., Vanden Berk, D. E., Reichard, T. A., Hall, P. B., Schneider, D. P.,
SubbaRao, M., Thakar, A. R., & York, D. G. 2002, AJ, 124, 1
- Sigut T.A. et al. 2004, ApJ, 611, 81
- Sulentic J. W. et al. 2000, AJ, 536, L5
- Sulentic J. W. et al. 2001, AIP Conference Proceedings, 599, 963
- Sulentic J. W. et al. 2002, ApJ, 566, 71
- Sulentic J. W. et al. 2006, RMxAA, 42, 23
- Sulentic J. W. et al. 2006b, A&A, 456, 929
- Sulentic J. W. et al. 2007, ApJ, 666, 757.
- Trevese, D., Paris, D., Stirpe, G. M., Vagnetti, F., and Zitelli, V. 2007, A&A, 470,
491
- Tytler, D., & Fan, X.-M. 1992, ApJS, 79, 1
- Vanden Berk et al. 2001, AJ, 122, 549

Verner E. et al. 2003, ApJ, 592, 59

Vestergaard M. and Peterson B.M. 2006, ApJ, 641, 689.

Vestergaard & Wilkes, 2001, ApJS, 134, 1

Wandel, A., Peterson, B. M., Malkan, M. 1999, ApJ, 526, 579

Woo, J.-H., et al. 2010, ApJ, 716, 269

Zamfir, S., Sulentic, J. W., Marziani, P., & Dultzin, D. 2010, MNRAS, 403, 1759

Table 1. Line Components in the $\lambda 1900$ blend

Ion	λ Å	X eV	$E_l - E_u$ eV	Transition	A s^{-1}	n_c cm^{-3}	Note
Si II	1808.00	8.15	0.000 - 6.857	$^2D_{3/2}^o \rightarrow ^2P_{1/2}$	$2.54 \cdot 10^6$...	1
Si II	1816.92	8.15	0.036 - 6.859	$^2D_{5/2}^o \rightarrow ^2P_{3/2}$	$2.65 \cdot 10^6$...	1
Al III	1854.716	18.83	0.000 - 6.685	$^2P_{3/2}^o \rightarrow ^2S_{1/2}$	$5.40 \cdot 10^8$...	1
Al III	1862.790	18.83	0.000 - 6.656	$^2P_{1/2}^o \rightarrow ^2S_{1/2}$	$5.33 \cdot 10^8$...	1
[Si III]	1882.7	16.34	0.000 - 6.585	$^3P_2^o \rightarrow ^1S_0$	0.012	$6.4 \cdot 10^4$	1,2,3
Si III]	1892.03	16.34	0.000 - 6.553	$^3P_1^o \rightarrow ^1S_0$	16700	$2.1 \cdot 10^{11}$	1,4,5
[C III]	1906.7	24.38	0.000 - 6.502	$^3P_2^o \rightarrow ^1S_0$	0.0052	$7.7 \cdot 10^4$	1,2,6
C III]	1908.734	24.38	0.000 - 6.495	$^3P_1^o \rightarrow ^1S_0$	114	$1.4 \cdot 10^{10}$	1,2,4,5
Fe III	1914.066	16.18	3.727 - 10.200	$z^7P_3^o \rightarrow a^7S_3$	$6.6 \cdot 10^8$...	7

Note. — All wavelengths are in vacuum. (1) Ralchenko, Yu., Kramida, A.E., Reader, J., and NIST ASD Team (2008). NIST Atomic Spectra Database (version 3.1.5). Available at: <http://physics.nist.gov/asd3>. 2: Feibelman & Aller (1987). 3: n_c computed following Shaw & Dufour (1995). 4: Morton (1991). 5: Feldman (1992). 6: Zheng (1988). 7: Wavelength and A from Ekberg (1993), energy levels from Edlén and Swings (1942).

Table 2. Basic Properties of Sources and Log of Observations

Object name	m_B	z	Line	M_B	Flux 6cm (mJy)	Date	DIT	N_{exp}	Airmass	S/N
(1)	(2)	(3)	(4)	(5)	(6)	(7)	(8)	(9)	(10)	(11)
J00103-0037	18.39	3.1546	1	-25.68	0.40	2006-11-08	1139	3	1.16, 1.13, 1.11	60
J00521-1108	18.70	3.2364	2	-25.39	0.43	2007-01-01	1199	3	1.15, 1.21, 1.29	41
J01225+1339	18.24	3.0511	1	-25.80	*	2006-11-08	1259	2	1.36, 1.32	92
J02287+0002	18.20	2.7282	1	-25.72	0.35	2006-12-16	1259	2	1.10, 1.12	67
J02390-0038	18.68	3.0675	2	-25.36	0.43	2006-11-07	1199	3	1.35, 1.46, 1.60	57
J03036-0023	17.65	3.2319	1	-26.44	0.34	2006-12-16	1259	2	1.11, 1.14	88
J20497-0554	18.29	3.1979	1	-25.79	*	2006-11-04	1259	2	1.52, 1.70	54
J23509-0052	18.67	3.0305	1	-25.36	0.41	2006-11-07	1199	3	1.10, 1.11, 1.14	62

*Not in FIRST

Table 3. Line Fluxes ^a

Object	CIII] λ 1909 ^b	SiIII] λ 1892	AlIII] λ 1860	SiII] λ 1814	CIV] λ 1549 _{BC}	CIV] λ 1549 _{blue}	CIV] λ 1549 _{VBC}	CIV] λ 1549 _{Tot}
J00103-0037	6.59 \pm 0.60	3.00 \pm 0.96	2.09 \pm 0.29	0.94 \pm 0.38 :	17.58 \pm 4.35	10.57 \pm 3.09	6.42 \pm 1.17	34.57 \pm 5.46
J00521-1108	3.56 \pm 1.98	3.21 \pm 1.27	1.85 \pm 1.09	1.17 \pm 0.85	12.46 \pm 2.73	2.50 \pm 1.20	6.57 \pm 1.70	21.53 \pm 3.43
J01225+1339	...	10.57 \pm 2.00	5.35 \pm 2.20	2.40 \pm 2.50	25.43 \pm 11.05	19.57 \pm 10.39	2.41 \pm 5.39 *	47.40 \pm 16.10
J02287+0002 ⁽¹⁾	6.49 \pm 0.40	2.96 \pm 0.93	2.05 \pm 0.79	1.25 \pm 0.85	13.95 \pm 1.98	3.36 \pm 0.30	0.50 \pm 0.48	17.80 \pm 2.06
J02287+0002 ⁽²⁾	5.69 \pm 0.43	4.71 \pm 0.62	2.52 \pm 0.62	1.30 \pm 0.65	9.13 \pm 2.37	10.21 \pm 0.35	0.48 \pm 0.69 *	19.82 \pm 2.50
J02390-0038	5.44 \pm 0.27	3.51 \pm 1.83	1.98 \pm 0.65	0.91 \pm 0.63	12.28 \pm 6.13	4.55 \pm 3.04	0.88 \pm 0.40	17.71 \pm 6.85
J03036-0023	...	14.71 \pm 4.79	6.95 \pm 2.63	3.02 \pm 2.85 :	31.64 \pm 14.99	19.70 \pm 7.79	4.82 \pm 4.52	56.15 \pm 17.49
J20497-0554	...	7.20 \pm 1.71	4.20 \pm 0.88	2.01 \pm 2.56 :	18.67 \pm 9.83	13.87 \pm 2.70	3.68 \pm 2.17	36.22 \pm 10.42
J23509-0052	...	3.95 \pm 1.68	1.76 \pm 1.17	0.72 \pm 1.12	10.24 \pm 2.30	9.30 \pm 2.53	2.15 \pm 1.41	21.69 \pm 3.70
Extreme Objects								
J12014+01161	...	17.44 \pm 2.66	15.50 \pm 3.34	6.47 \pm 3.27	25.06 \pm 6.15	32.30 \pm 15.11	0.49 \pm 3.70 *	57.85 \pm 16.73
3C 390.3	5.86 \pm 0.62	4.05 \pm 0.57	0.36 \pm 0.28	0.50 \pm 0.41	52.99 \pm 6.85	12.81 \pm 3.00	38.74 \pm 4.45	104.54 \pm 8.70

Note. — (a) Units are 10^{-14} ergs s⁻¹ cm⁻² Å⁻¹. (b) We do not report values of CIII] λ 1909 for Pop. and boundary objects. See text for explanation. (1) Using CIII] λ 1909 to place the restframe. (2) Using OI] λ 1304 to place the restframe. (:): Approximated values due the line is affected by telluric absorptions (see Fig. 1). (*) Consistent with no emission.

Table 4. Equivalent Widths

Object	CIII] λ 1909 ^a	SIII] λ 1892	AlIII] λ 1860	SIII] λ 1814	CIV] λ 1549 _{BC}	CIV] λ 1549 _{Tot}
J00103-0037	18.0 \pm 2.0	8.1 \pm 5.0	5.5 \pm 2.0	2.4 \pm 2.1 :	35.2 \pm 17.9	69.3 \pm 21.6
J00521-1108	9.5 \pm 5.3	8.4 \pm 4.0	4.7 \pm 3.3	2.9 \pm 2.4	24.8 \pm 7.2	42.4 \pm 8.8
J01225+1339	...	15.0 \pm 4.0	7.4 \pm 3.8	3.2 \pm 3.8	28.2 \pm 14.2	52.8 \pm 15.7
J02287+0002 ⁽¹⁾	19.6 \pm 2.9	8.9 \pm 3.6	6.1 \pm 2.0	3.7 \pm 1.9	37.4 \pm 7.5	47.8 \pm 7.7
J02287+0002 ⁽²⁾	17.1 \pm 2.7	14.1 \pm 3.1	7.5 \pm 1.8	3.8 \pm 2.3	24.5 \pm 7.1	53.1 \pm 7.2
J02390-0038	16.6 \pm 3.2	10.6 \pm 3.4	5.8 \pm 2.0	2.6 \pm 1.8	26.8 \pm 5.8	38.6 \pm 6.0
J03036-0023	...	13.5 \pm 4.9	6.2 \pm 2.7	2.6 \pm 2.6 :	21.1 \pm 11.0	37.6 \pm 12.1
J20497-0554	...	13.6 \pm 3.0	7.8 \pm 1.7	4.5 \pm 1.8 :	26.3 \pm 14.0	50.8 \pm 14.9
J23509-0052	...	12.1 \pm 6.6	5.3 \pm 4.3	2.1 \pm 3.7	25.0 \pm 8.0	52.8 \pm 12.2
Extreme Objects						
J12014+01161	...	9.2 \pm 2.0	8.0 \pm 2.2	3.2 \pm 1.8	9.6 \pm 2.9	22.1 \pm 5.5
3C 390.3	42.4 \pm 3.6	14.2 \pm 2.5	1.2 \pm 1.2	1.5 \pm 1.4	88.5 \pm 8.2	179.6 \pm 10.0

Note. — (a) We do not report values of CIII] λ 1909 for Pop. and boundary objects. See text for explanation.
(1) Using CIII] λ 1909 to place the restframe. (2) Using OI] λ 1304 to place the restframe. (:): Approximated values due the line is affected by telluric absorptions.

Table 5. Broad Components Intensity Ratios used to compute n_e and U.

Object	$\text{Log}(\text{AlIII}\lambda 1860 / \text{SiII}\lambda 1892)$	$\text{Log}(\text{CIV}\lambda 1549_{BC} / \text{AlIII}\lambda 1860)$	$\text{Log}(\text{SiII}\lambda 1814 / \text{SiII}\lambda 1892)$
J00103-0037	-0.16 ± 0.15	0.92 ± 0.12	-0.50 ± 0.22 :
J00521-1108	-0.24 ± 0.31	0.83 ± 0.27	-0.44 ± 0.36
J01225+1339	-0.30 ± 0.20	0.68 ± 0.26	-0.64 ± 0.46
J02287+0002 ⁽¹⁾	-0.16 ± 0.22	0.83 ± 0.18	-0.37 ± 0.33
J02287+0002 ⁽²⁾	-0.27 ± 0.12	0.56 ± 0.16	-0.56 ± 0.22
J02390-0038	-0.25 ± 0.27	0.79 ± 0.26	-0.59 ± 0.38
J03036-0023	-0.33 ± 0.22	0.66 ± 0.26	-0.69 ± 0.43 :
J20497-0554	-0.23 ± 0.14	0.65 ± 0.25	-0.55 ± 0.56 :
J23509-0052	-0.35 ± 0.34	0.76 ± 0.30	-0.74 ± 0.70
Extreme Objects			
J12014+01161	-0.05 ± 0.11	0.21 ± 0.14	-0.43 ± 0.23 $\text{log}(\text{CIII}\lambda 1909 / \text{SiII}\lambda 1892)$
3C 390.3	-1.05 ± 0.34	2.17 ± 0.34	0.16 ± 0.08

Note. — (1) Using OI $\lambda 1304$ to place the restframe. (2) Using CIII $\lambda 1909$ to place the restframe. (:) SiII $\lambda 1814$ is affected by telluric absorptions.

Table 6. Electron Density and Ionization Parameter

Object	$\text{Log}n_e$	$\text{Log}U$
J00103-0037	12.48 ± 0.42	-2.69 ± 0.23
J00521-1108	12.44 ± 0.20	-2.85 ± 0.17
J01225+1339	12.35 ± 0.27	-2.78 ± 0.40
J01225+1339 †	11.99 ± 0.22	-2.53 ± 0.33
J02287+0002 ⁽¹⁾	12.54 ± 0.20	-2.84 ± 0.18
J02287+0002 ⁽²⁾	12.44 ± 0.26	-2.90 ± 0.21
J02390-0038	12.36 ± 0.18	-2.78 ± 0.30
J03036-0023	12.42 ± 0.25	-3.02 ± 0.20
J03036-0023 †	11.95 ± 0.21	-2.54 ± 0.27
J20497-0554	12.56 ± 0.17	-3.03 ± 0.21
J20497-0554 †	12.15 ± 0.13	-2.54 ± 0.27
J23509-0052	12.23 ± 0.43	-2.67 ± 0.32
J23509-0052 †	11.84 ± 0.27	-2.41 ± 0.33
Extreme Objects		
J12014+01161	12.85 ± 0.30	-2.99 ± 0.51
J12014+01161†	12.69 ± 0.35	-2.85 ± 0.60
3C 390.3	9.98 ± 0.50	-1.47 ± 0.37

Note. — (†) Values of electron density and ionization parameter computed assuming metallicity $Z = 5Z_{\odot}$. (1) Using O I $\lambda 1304$ to place the restframe. (2) Using C III $\lambda 1909$ to place the restframe.

Table 7. Parameters from the fits, the size of the Broad Line Region and the Black Hole masses.

Object	d_p $X 10^{28} [\text{cm}]$	$f(1700\text{\AA})^a$ $X 10^{-15}$	$f(1350\text{\AA})^a$ $X 10^{-15}$	FWHM(BC) [km s^{-1}]	Pop.	$\text{Log}(n_e \cdot U)$	$\text{Log}(r_{BLR})^b$ [cm]	$\text{Log}(M_{BH})^b$ [M_\odot]	$\text{Log}(M_{BH})^c$ V&P (2006)
(1)	(2)	(3)	(4)	(5)	(6)	(7)	(8)	(9)	(10)
J00103-0037	2.01	4.9 ± 1.0	6.6 ± 1.3	4700 ± 1200	B	9.79 ± 0.42	18.03 ± 0.22	9.40 ± 0.31	9.41
J00521-1108	2.03	6.6 ± 1.6	8.9 ± 2.1	6100 ± 3000	B	9.59 ± 0.22	18.13 ± 0.13	9.72 ± 0.45	9.71
J01225+1339	1.98	8.9 ± 1.8	12.2 ± 2.4	4300 ± 1200	B*	9.57 ± 0.41	18.29 ± 0.21	9.57 ± 0.32	9.47
J01225+1339 †						9.46 ± 0.34	18.34 ± 0.18	9.63 ± 0.30	
J02287+0002 ⁽¹⁾	1.87	7.4 ± 2.7	8.4 ± 3.0	5700 ± 800	B	9.70 ± 0.23	18.01 ± 0.14	9.55 ± 0.19	9.61
J02287+0002 ⁽²⁾	1.87	7.4 ± 2.7	8.4 ± 3.0	5200 ± 800		9.54 ± 0.28	18.09 ± 0.16	9.54 ± 0.21	9.52
J02390-0038	1.99	6.8 ± 2.0	9.4 ± 2.8	8200 ± 1600	B	9.58 ± 0.31	18.11 ± 0.17	9.96 ± 0.24	9.98
J03036-0023	2.03	20.5 ± 5.7	30.0 ± 8.4	3600 ± 800	A	9.40 ± 0.27	18.46 ± 0.15	9.60 ± 0.25	9.53
J03036-0023 †						9.41 ± 0.30	18.46 ± 0.16	9.59 ± 0.25	
J20497-0554	2.02	6.8 ± 1.4	9.9 ± 2.0	3900 ± 2000	A	9.53 ± 0.23	18.25 ± 0.13	9.45 ± 0.46	9.34
J20497-0554 †						9.61 ± 0.27	18.21 ± 0.14	9.41 ± 0.47	
J23509-0052	1.97	4.7 ± 0.9	6.0 ± 1.2	4600 ± 1400	B*	9.57 ± 0.46	18.10 ± 0.23	9.44 ± 0.35	9.36
J23509-0052 †						9.43 ± 0.37	18.17 ± 0.19	9.51 ± 0.33	
Extreme Objects									
J12014+01161	2.03	22.1 ± 1.5	32.2 ± 2.2	4000 ± 1400	A	9.86 ± 0.52	18.35 ± 0.26	9.58 ± 0.40	9.64
J12014+01161†						9.84 ± 0.60	18.29 ± 0.30	9.52 ± 0.43	
3C 390.3	0.07	3.9 ± 1.3	9.4 ± 2.6	8400 ± 1000	B	8.51 ± 0.54	17.24 ± 0.28	9.11 ± 0.30	8.48

Note. — (a) Units of the flux at 1350 and 1700Å are in $\text{ergs s}^{-1} \text{cm}^{-2} \text{Å}^{-1}$. (b) The showed values of the size of the BLR and the black hole mass M_{BH} are the average ± 0.17 of the computation using both SED of Laor (1997) and Mathews & Ferland (1987) (see Fig. 15). (c) We show the comparison between our computations and those using the Vestergaard & Peterson (2006) mehtod. They report an uncertainty of 0.66 dex. Units are in solar mases M_{\odot} . (†) Values of electron density and ionization parameter computed assuming metalicity $Z = 5Z_{\odot}$. (1) Using OI $\lambda 1304$ to place the restframe. (2) Using CIII] $\lambda 1909$ to place the restframe. (*) Objects in the boundary of Pop. A to B.

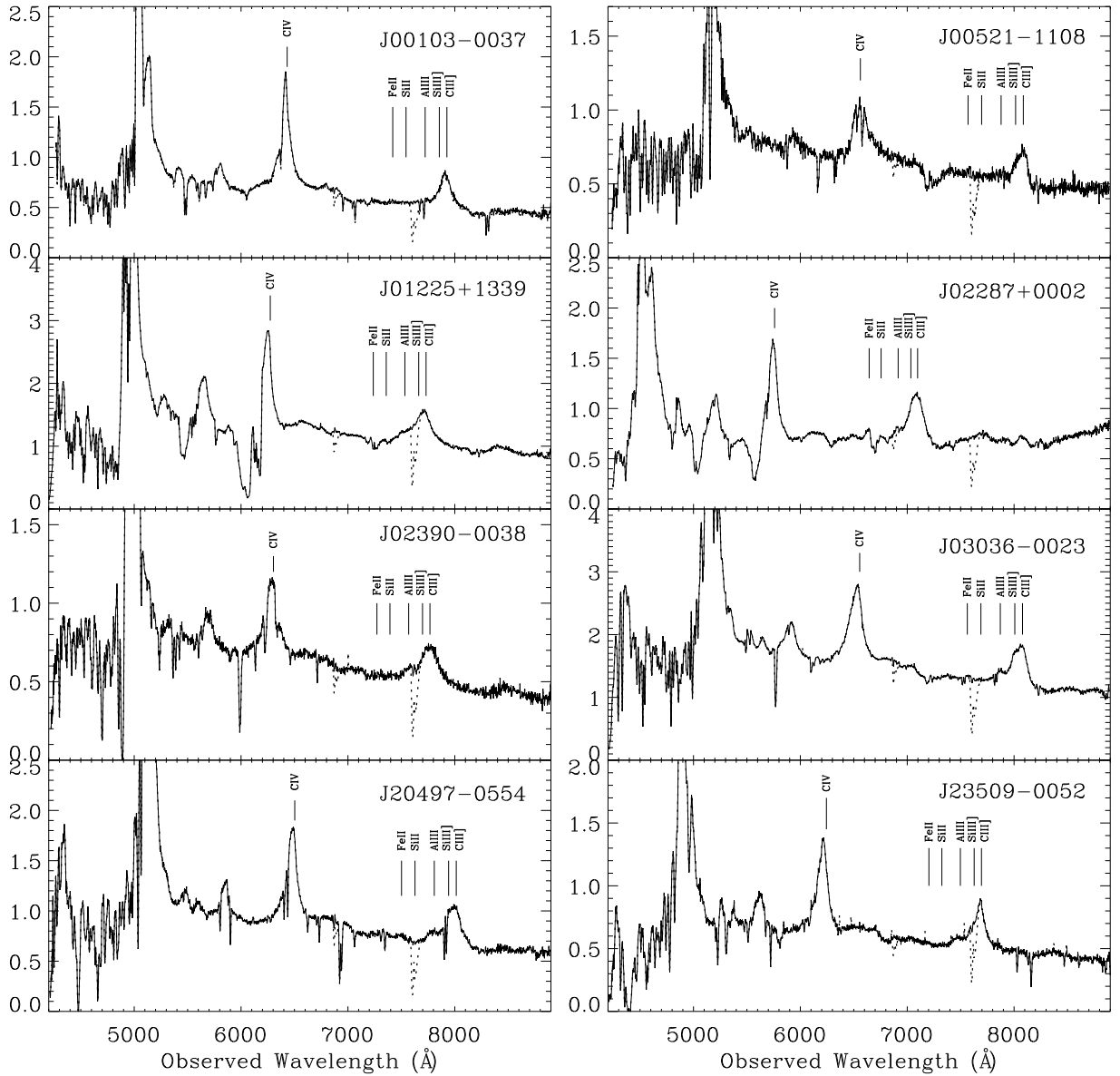


Fig. 1.— Sample of 8 VLT spectra. Abscissa is observed wavelength in \AA , ordinate is specific flux in units $10^{-16} \text{ ergs s}^{-1} \text{ cm}^{-2} \text{ \AA}^{-1}$. The superimposed dotted line is before atmospheric bands subtraction. We show the positions of the lines of our interest $\text{CIII}\lambda 1909$, $\text{SiIII}\lambda 1892$, $\text{AlIII}\lambda 1860$, $\text{SiII}\lambda 1814$, $\text{FeII}\lambda 1787$ and $\text{CIV}\lambda 1549$. J01225+1339 and J02287 are BAL quasars.

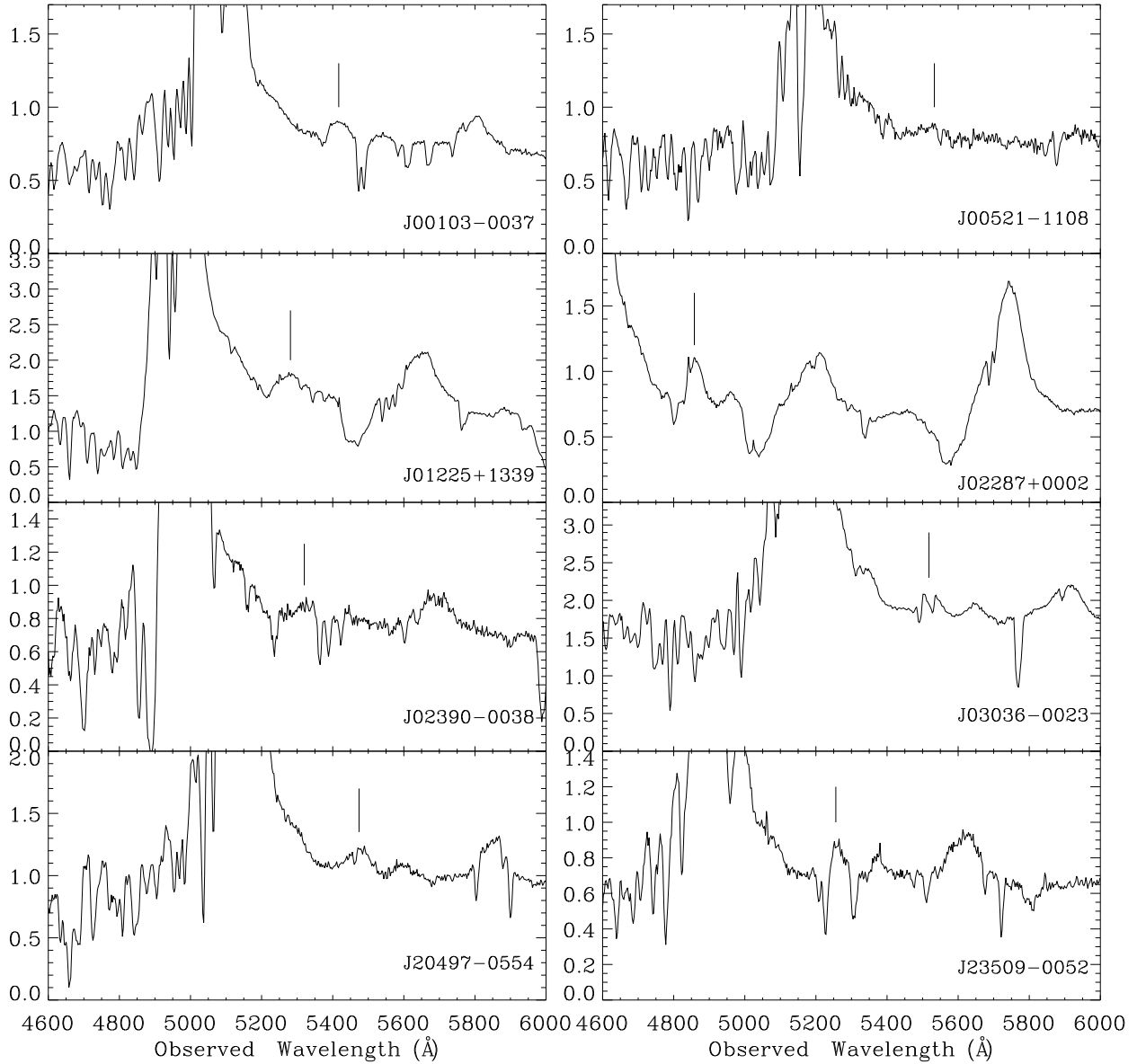


Fig. 2.— $O\text{I}\lambda 1304.8$ used to place the restframe showed by the mark. Abscissa is rest frame wavelength in \AA , ordinate is specific flux in units $10^{-16} \text{ ergs s}^{-1} \text{ cm}^{-2} \text{ \AA}^{-1}$. In J00521-1108 and J02390-0038 the peak of $O\text{I}\lambda 1304.8$ is not observed clearly. In J00103-0037, J02287+0002 and J20497-0554, the redshift results, using both $O\text{I}\lambda 1304.8$ and $\text{CIII]}\lambda 1909$, are ambiguous. In J01225+1339, J03036-0023 and J23509-0052, the redshifts obtained using $O\text{I}\lambda 1304.8$ or $\text{CIII]}\lambda 1909$ are consistent.

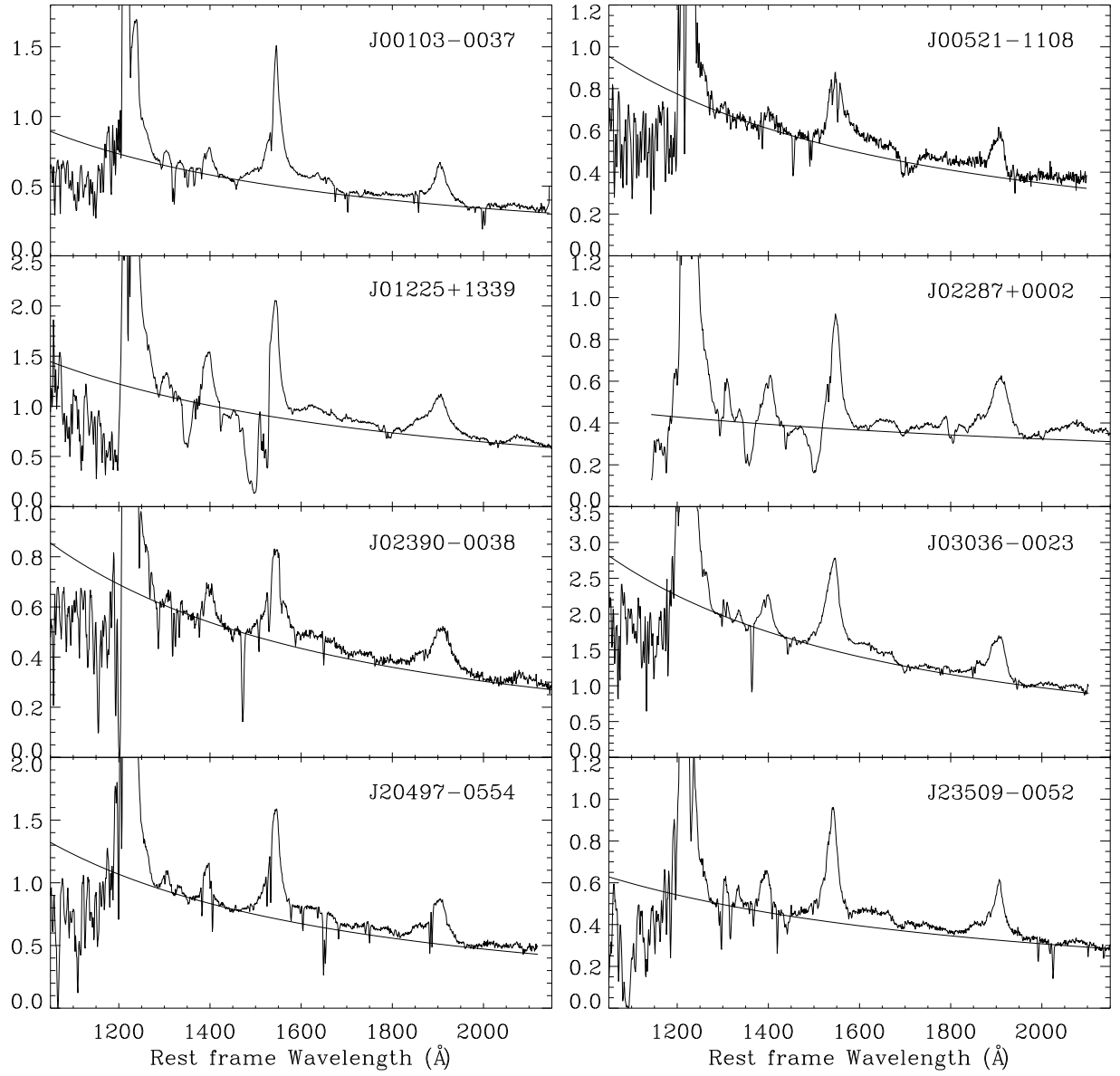


Fig. 3.— Sample of 8 VLT spectra in rest frame wavelength. Abscissa is rest frame in \AA , ordinate is specific flux in units 10^{-14} ergs s^{-1} cm^{-2} \AA^{-1} .

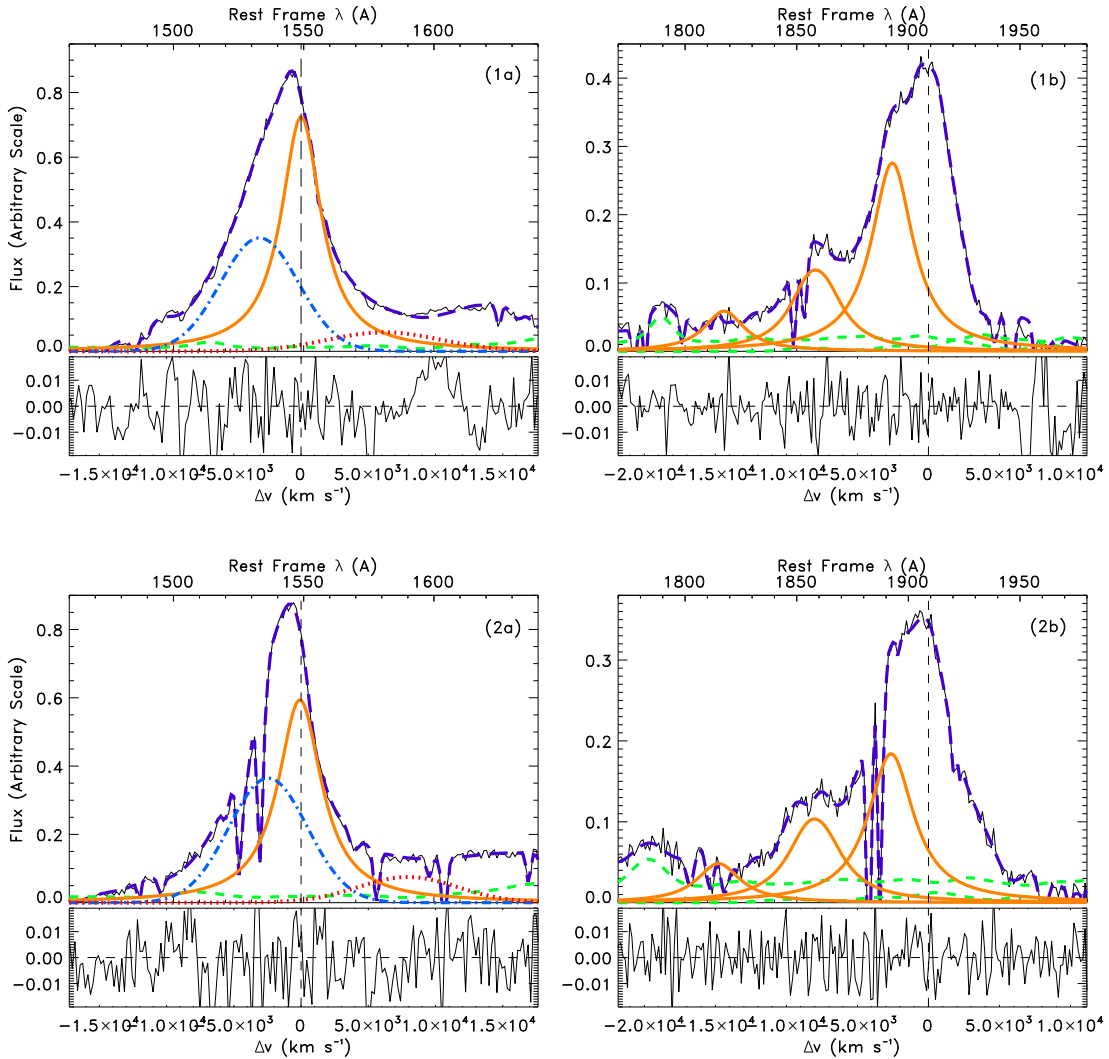


Fig. 4.— Fits for Pop. A objects (1) J03036-0023, (2) J20497-0554. Upper abscissa is rest frame wavelength in Å, lower abscissa is in velocity units, ordinate is specific flux in arbitrary units. Short dashed line is the restframe for (a) CIV λ 1549 and (b) CIII] λ 1909. Long dashed line is the fit, solid line are the broad components: CIV λ 1549 in (a) and SiII] λ 1892, AlII] λ 1860, SiII] λ 1814 in (b). Dot-dashed line in (b) is the blue-shifted component of CIV λ 1549 while dotted line is the very broad component. Pannels under the fits are the residuals.

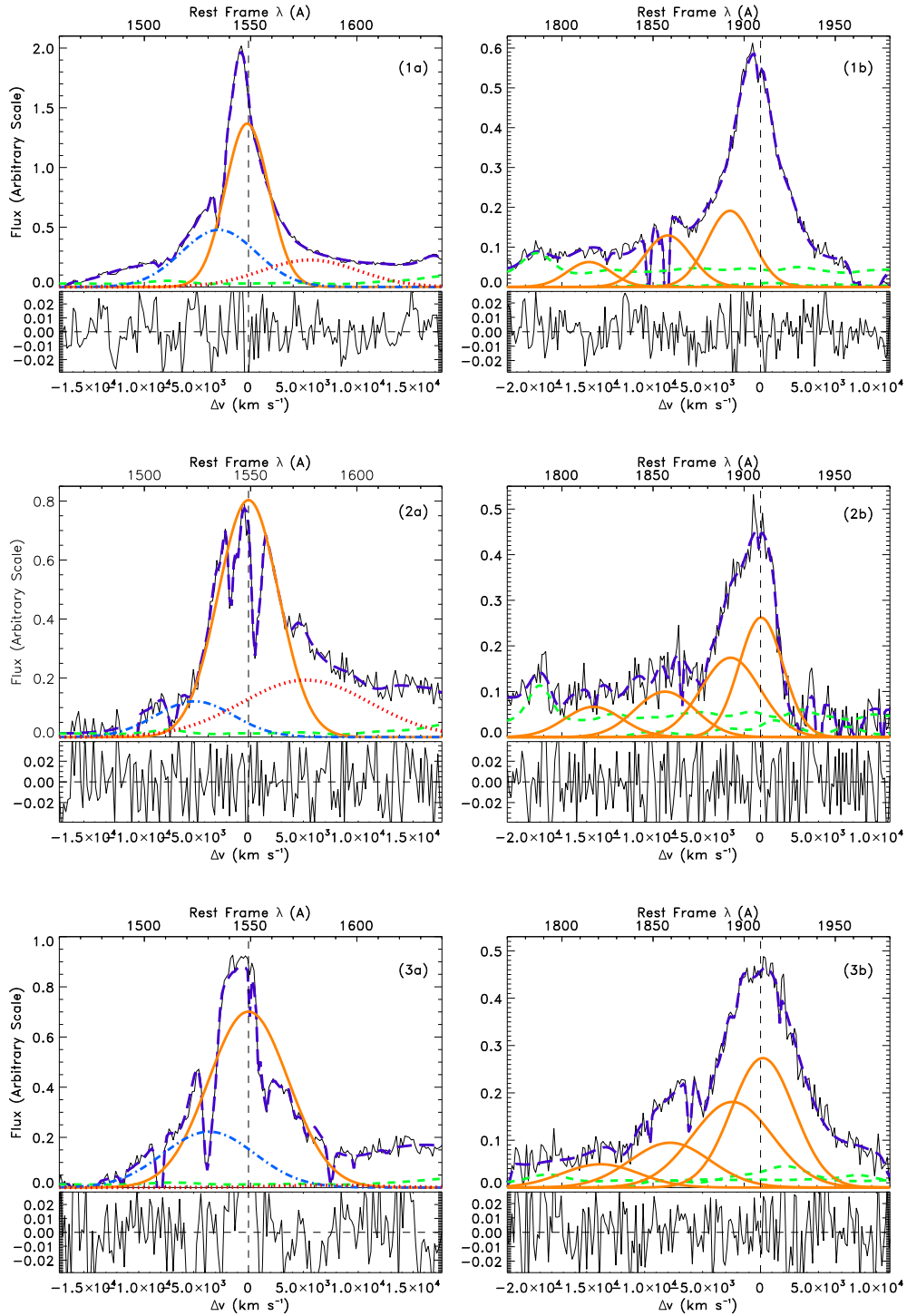


Fig. 5.— Fits for Pop. B objects (1) J00103-0037, (2) J00521-1108, (3) J02390-0038. Units and meaning of symbols are the same of fig. 4. For these objects we show C III] λ 1909 component.

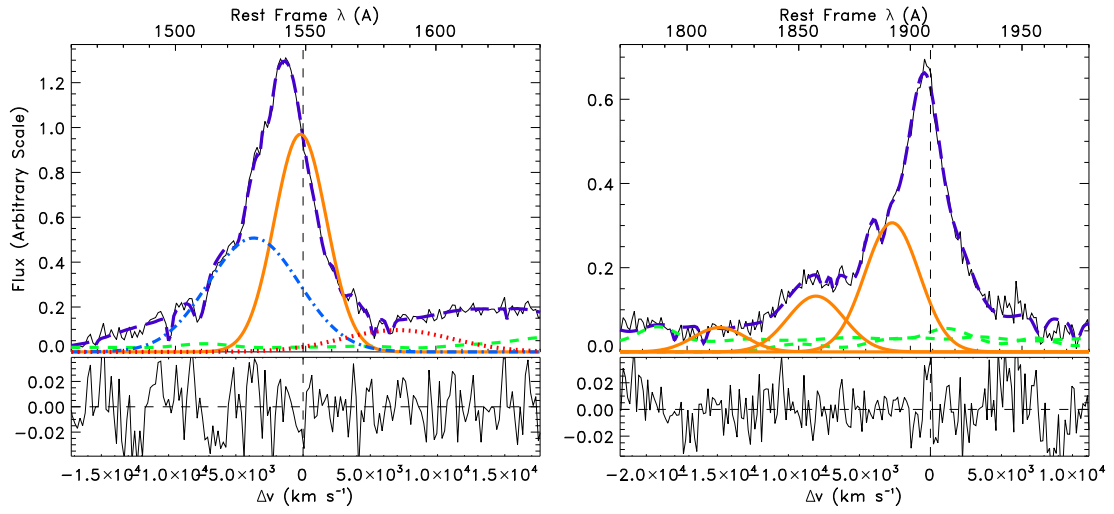


Fig. 6.— Fit for J23509-0052 which is in the boundary of Pop. A to B. Units and meaning of symbols are the same of fig. 4.

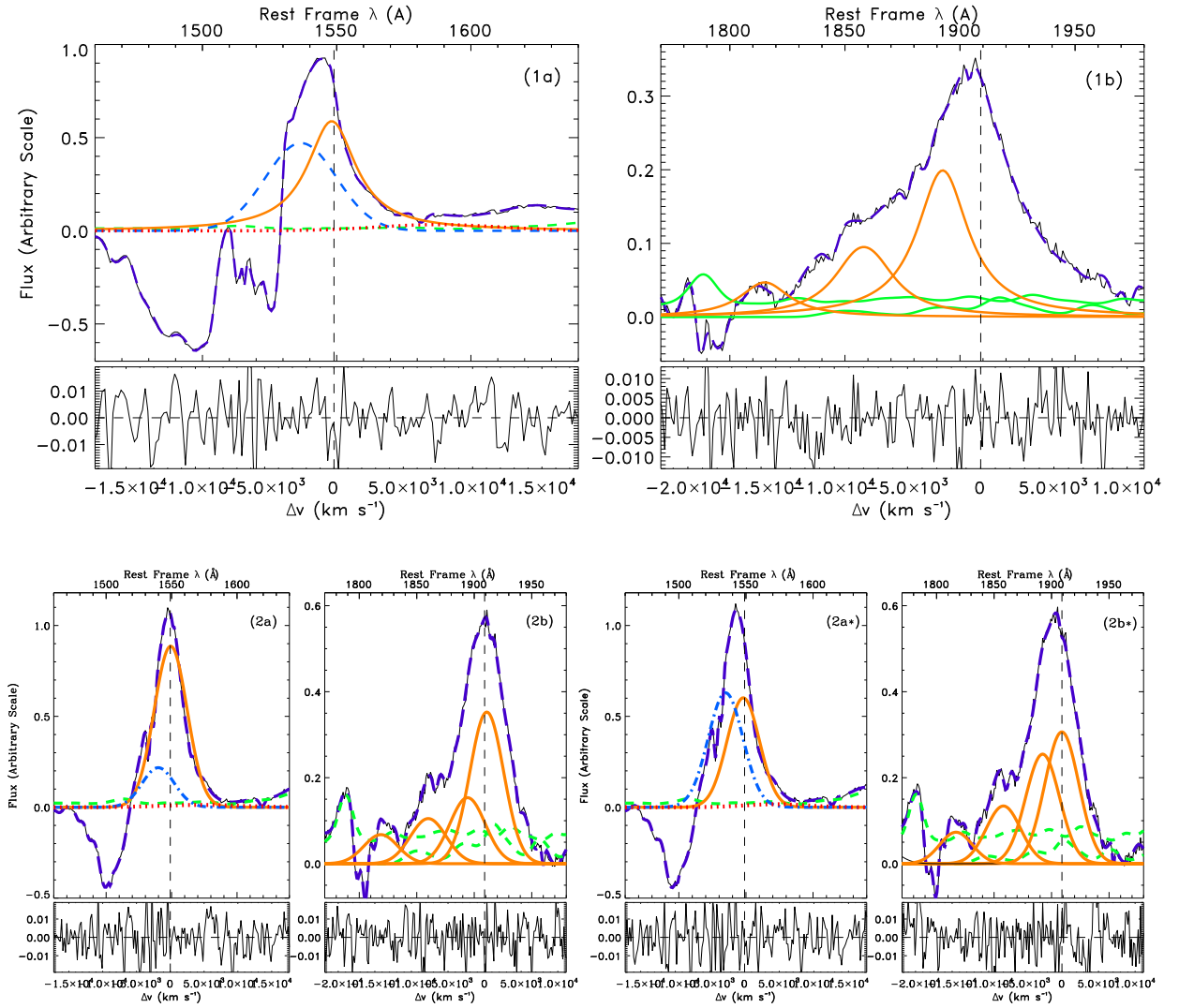


Fig. 7.— Fits for BAL quasars (1) J01225+1339 and (2) J02287+0002. Units and meaning of symbols are the same of fig. 4. For (2a) and (2b) z_{ciii} was used to place the restframe. For (2a*) and (2b*) z_{oi} was used. Note in J02287+0002 the line displacement with the consequently line intensity changes, specially in CIII] λ 1909, SiIII] λ 1892 and CIV] λ 1549 broad and blue-shifted components. For J02287+0002 we show CIII] λ 1909 component.

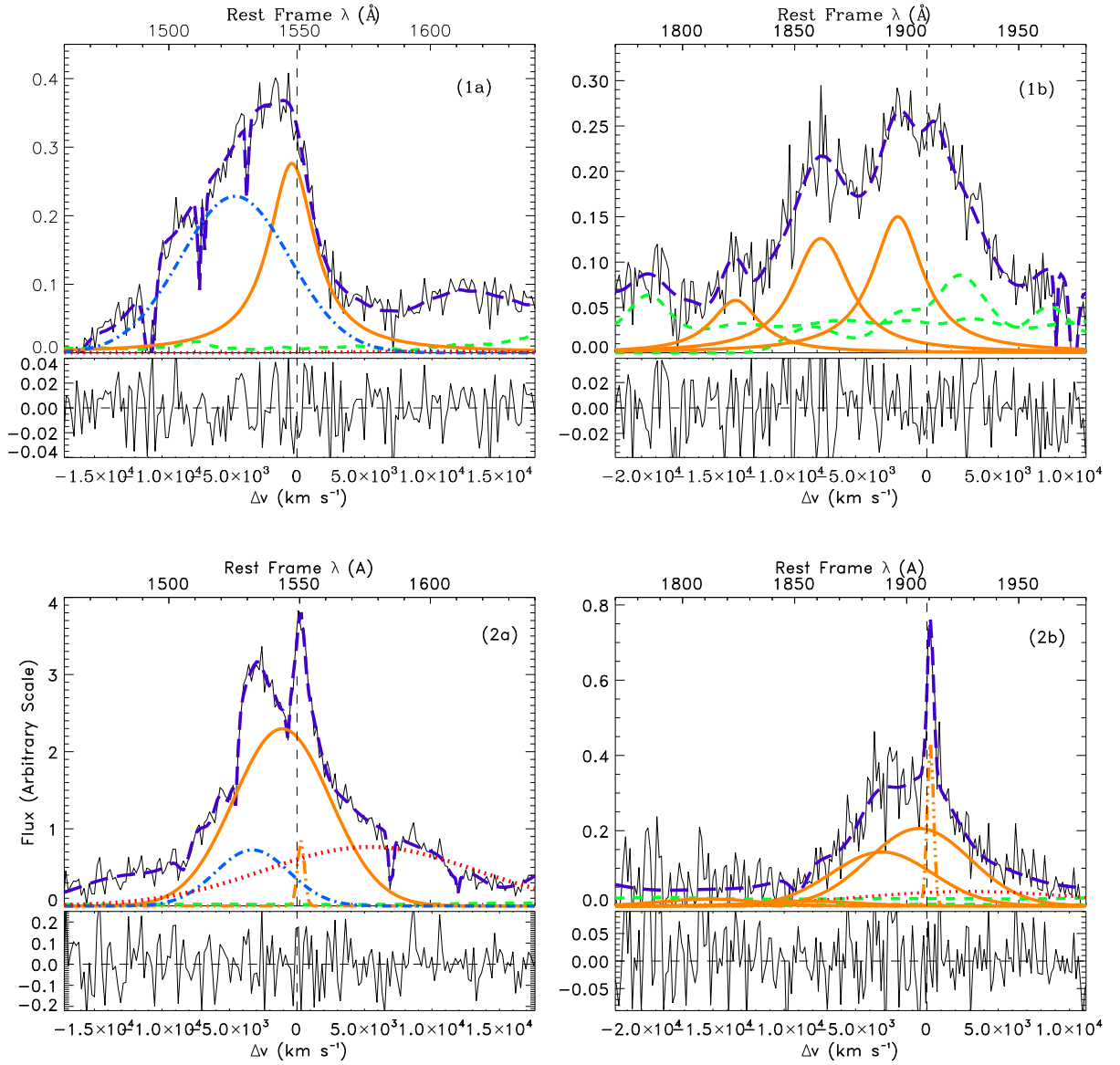


Fig. 8.— Fits for the two extreme objects (1) J120144.36+011611.6 and (2) 3C390.3. Units and meaning of symbols are the same of fig. 4. For 3C390.3 it was needed to fit a narrow unshifted component that we show in dash-dot-dot line. In (2b) we show $\text{CIII}] \lambda 1909_{BC}$ which is used to compute n_e and U (see table 5) and dotted line is $\text{CIII}] \lambda 1909_{VBC}$. Note for 3C390.3 $\text{SiII} \lambda 1814$ is almost absent.

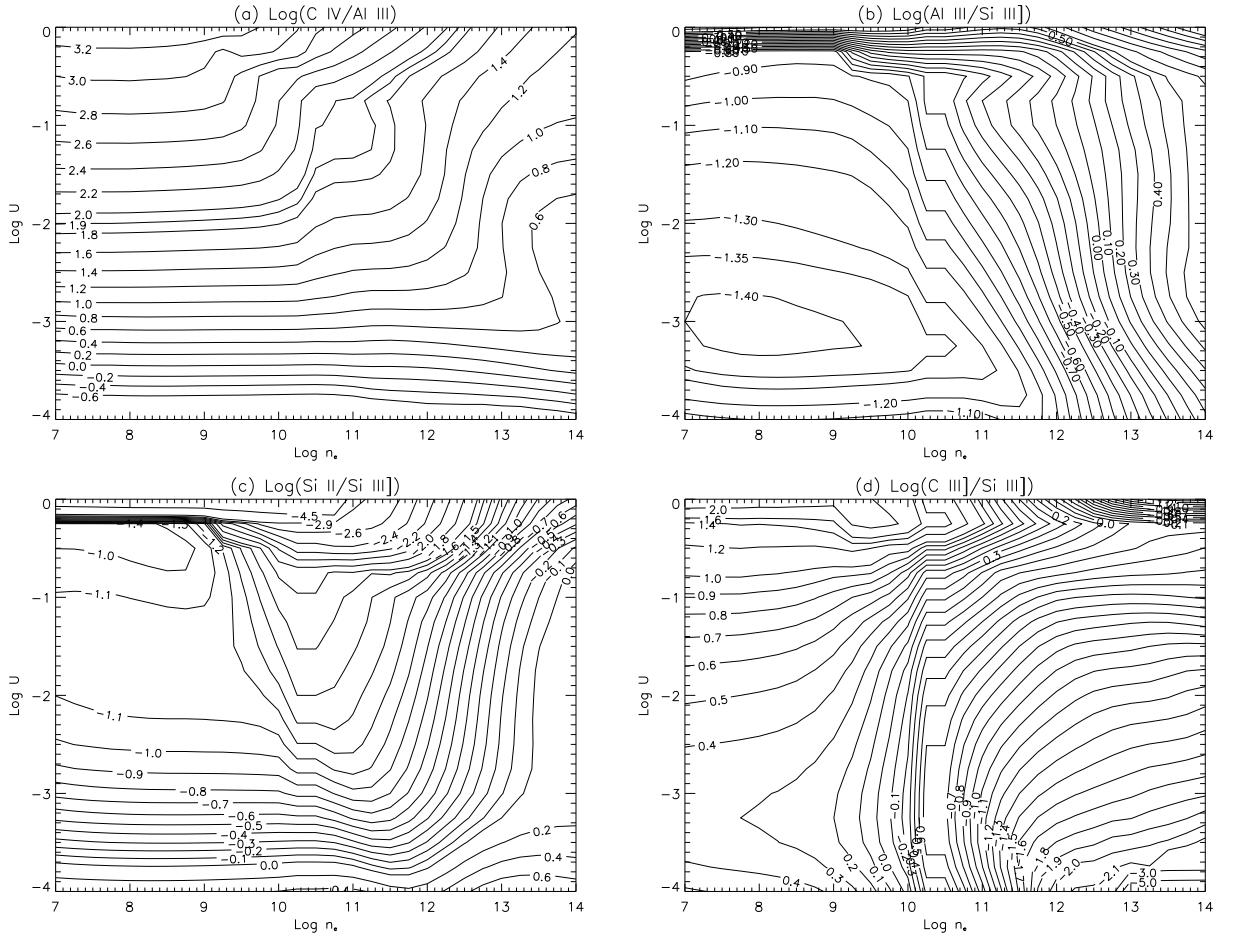


Fig. 9.— Isocontours for the ratios (a) $\text{Log}(\text{C IV } \lambda 1549 / \text{Al III } \lambda 1860)$, (b) $\text{Log}(\text{Al III } \lambda 1860 / \text{Si III } \lambda 1892)$, (c) $\text{Log}(\text{Si II } \lambda 1814 / \text{Si III } \lambda 1892)$ and (d) $\text{Log}(\text{C III } \lambda 1909 / \text{Si III } \lambda 1892)$ derived from CLOUDY simulations. Abscissa is electron density in cm^{-3} , ordinate is the ionization parameter, both in logarithm scale.

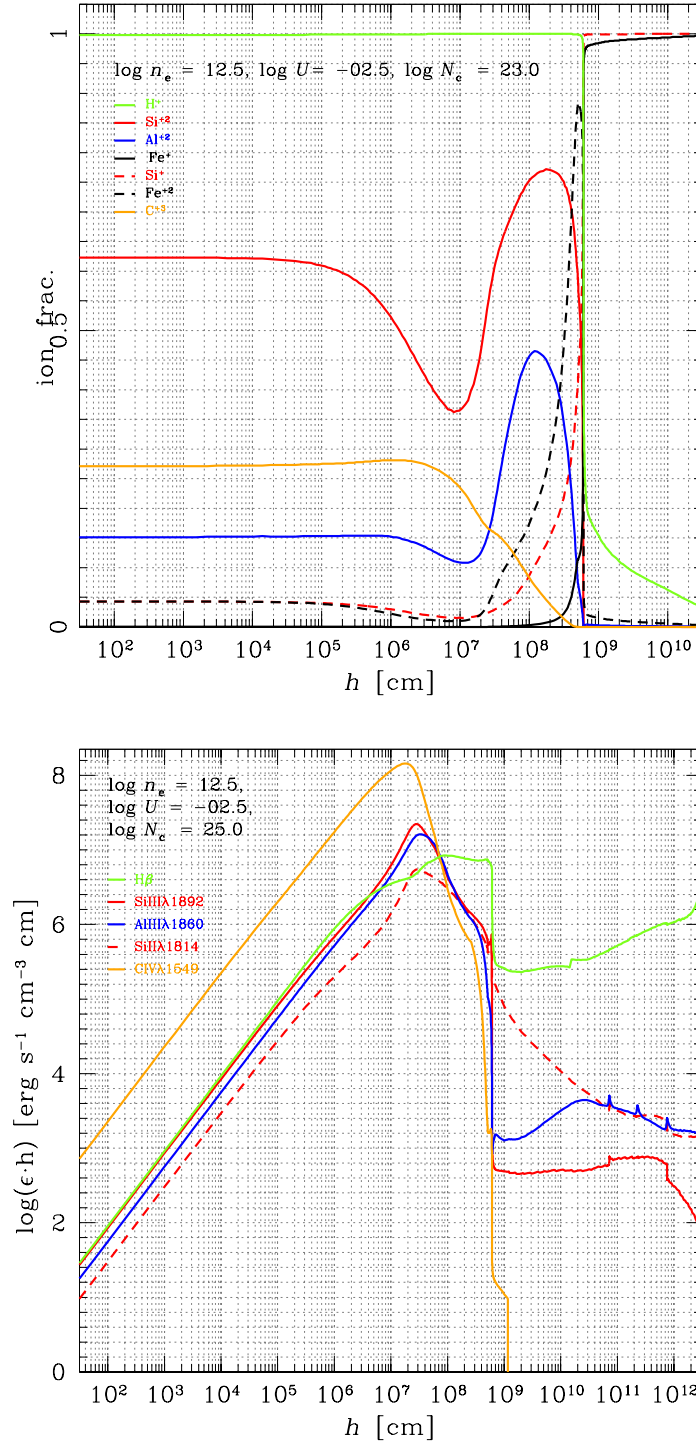


Fig. 10.— Top: Ionic Fractions as a function of the geometric depth h in the gas slab. Bottom: Line emissivity per unit volume in units of ergs s⁻¹ cm⁻³ multiplied by depth.

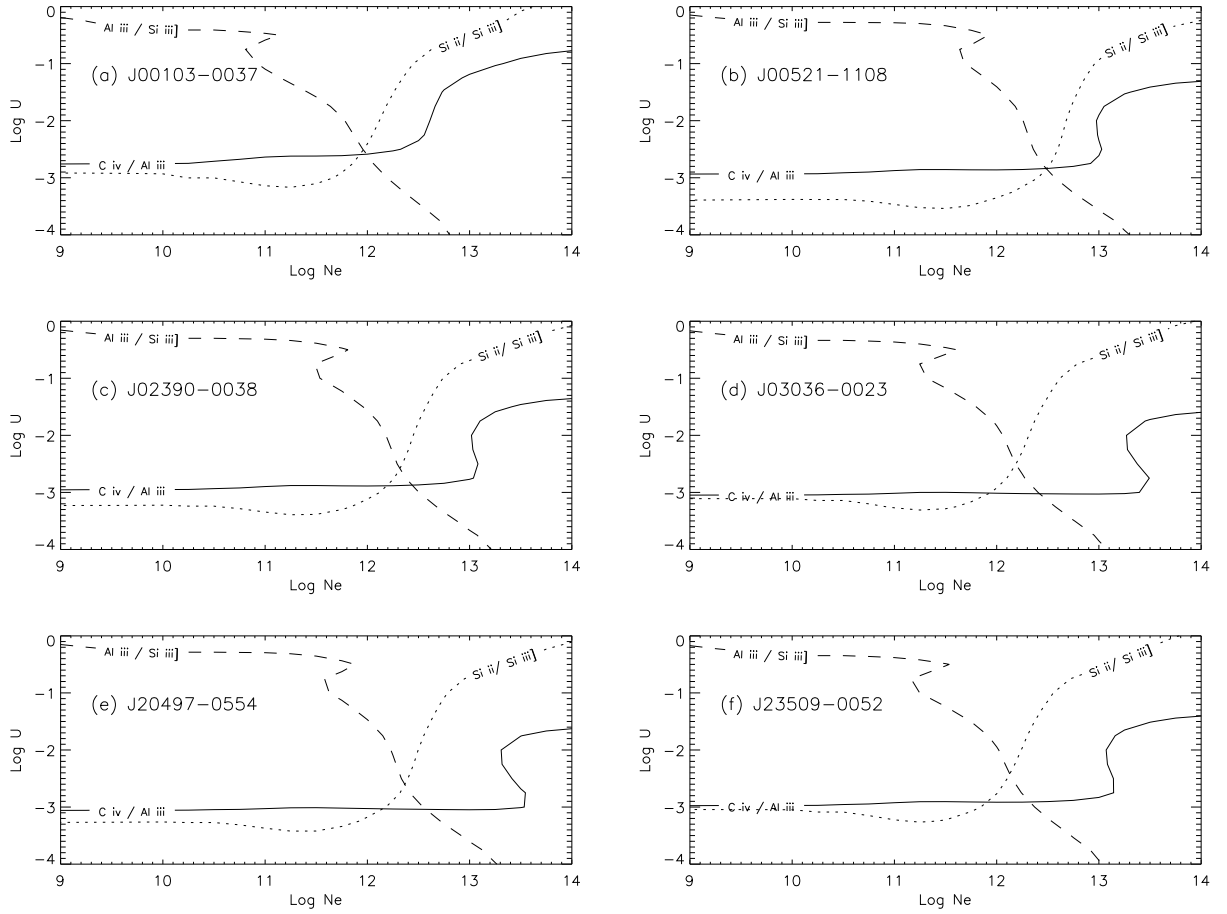


Fig. 11.— Contour plots for (a) J00103-0037, (b) J00521-1108, (c) J02390-0038, (d) J03036-0023, (e) J20497-0554 and (f) 23509-0052. Abscissa is electron density in cm^{-3} , ordinate is the ionization parameter, both in logarithm scale. Solid line is for $\text{Log}(C\text{ iv } \lambda 1549 / Al\text{ iii } \lambda 1860)$ ratio, dashed line is for $\text{Log}(Al\text{ iii } \lambda 1860 / Si\text{ iii } \lambda 1892)$ ratio, dotted line is for $\text{Log}(Si\text{ ii } \lambda 1814 / Si\text{ iii } \lambda 1892)$ ratio. The point where the isocontours cross determine the values of $\text{Log}n_e$ and $\text{Log}U$.

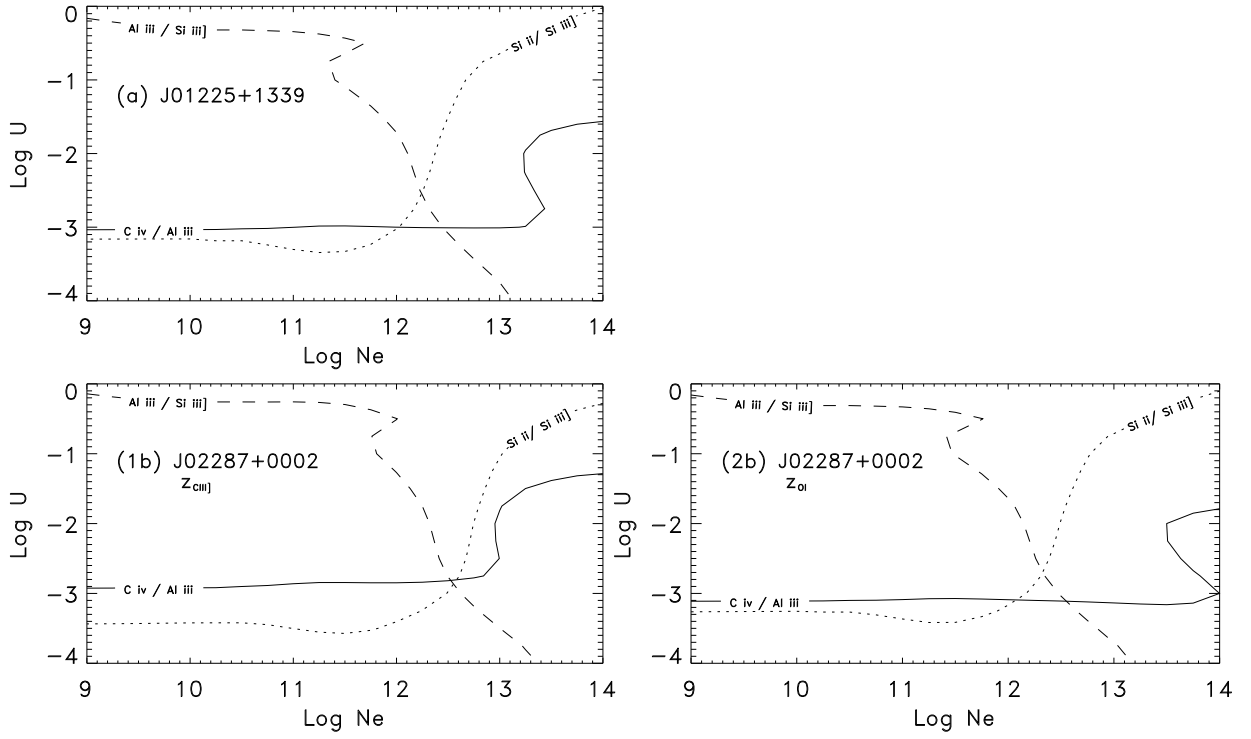


Fig. 12.— Contour plots for BAL quasars (a) J01225+1339 and (b) J02287+0002. In (1b) z_{CIII} was used to place the restframe. In (2b) we use z_{OI} . Units and meaning of symbols are the same of Fig. 11.

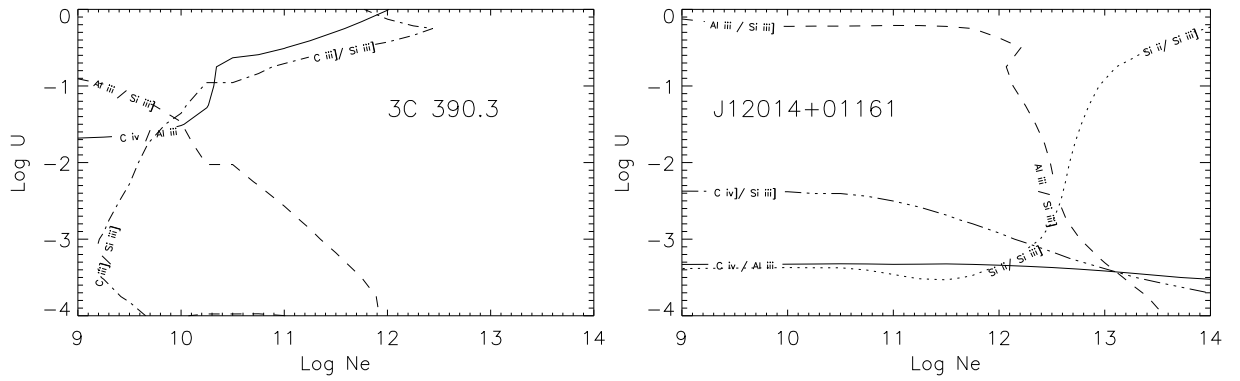


Fig. 13.— Contour plots for the extreme objects 3C390.9 and J12014+0116. Units and meaning of symbols are the same of Fig. 11. In 3C390.3 we add a dashed-dotted line for $\text{Log}(\text{CIII}\lambda 1909 / \text{SiIII}\lambda 1892)$ ratio and in J12014+0116 a dashed-triple dotted line for $\text{Log}(\text{CIV}\lambda 1549 / \text{SiIII}\lambda 1892)$ ratio. See text for further details.

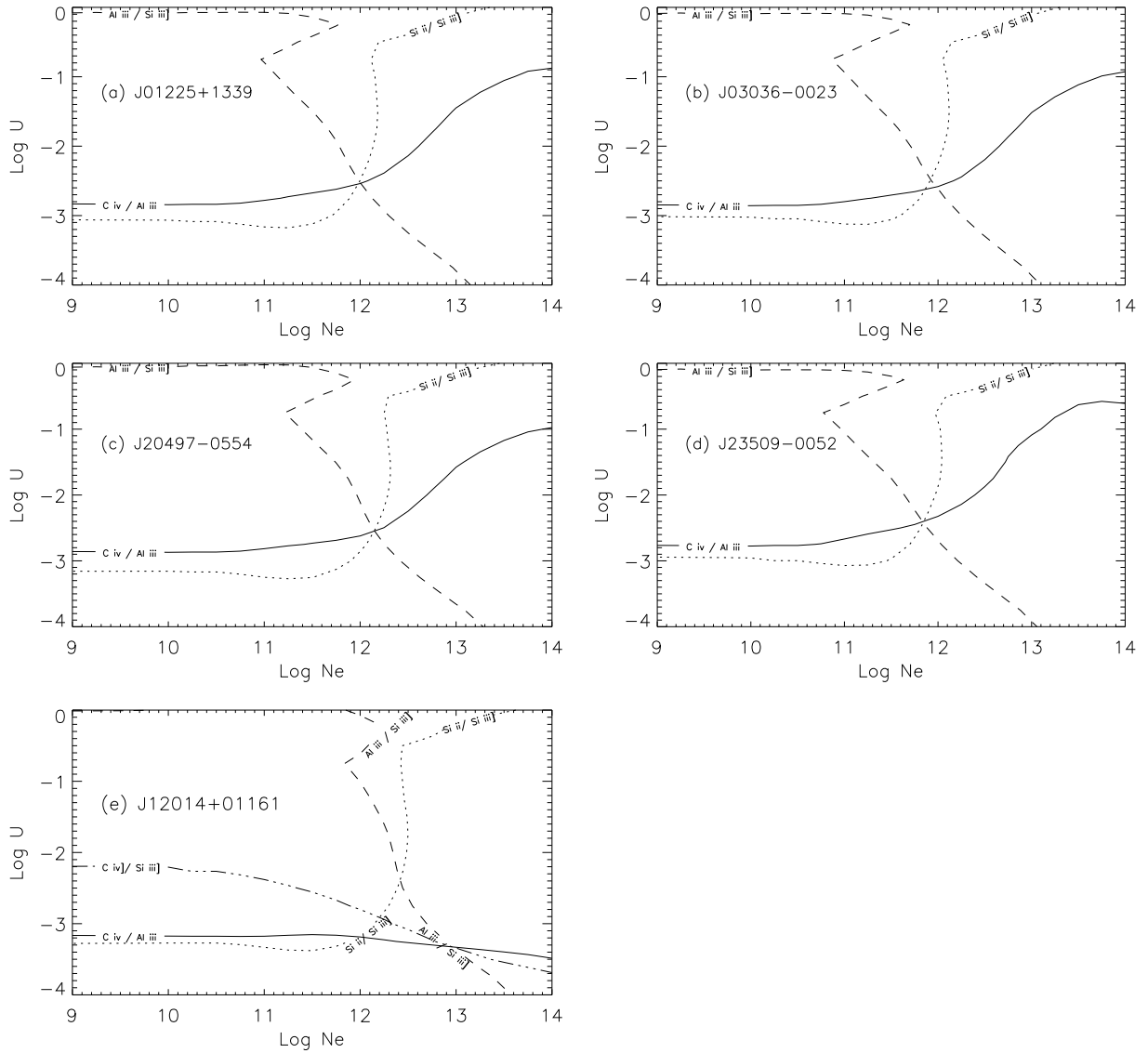


Fig. 14.— Contour plots for (a) BAL quasar J01225+1339, (b) J03036-0023, (c) J20497-0554, (d) J23509-0052 and the extreme object (e) J12014+0116 from the array of simulations computed for $Z = 5Z_{\odot}$. Coordinates and symbols are as for Fig. 11. In (e) we added a dashed-triple dotted line for $\text{Log}(\text{CIV}\lambda 1549 / \text{SiII}\lambda 1892)$ ratio. The intersection point is concordant in (a) to (d) cases, unlike when $Z = Z_{\odot}$ was assumed. For (e), the agreement is better than $Z = Z_{\odot}$ of figure 13.

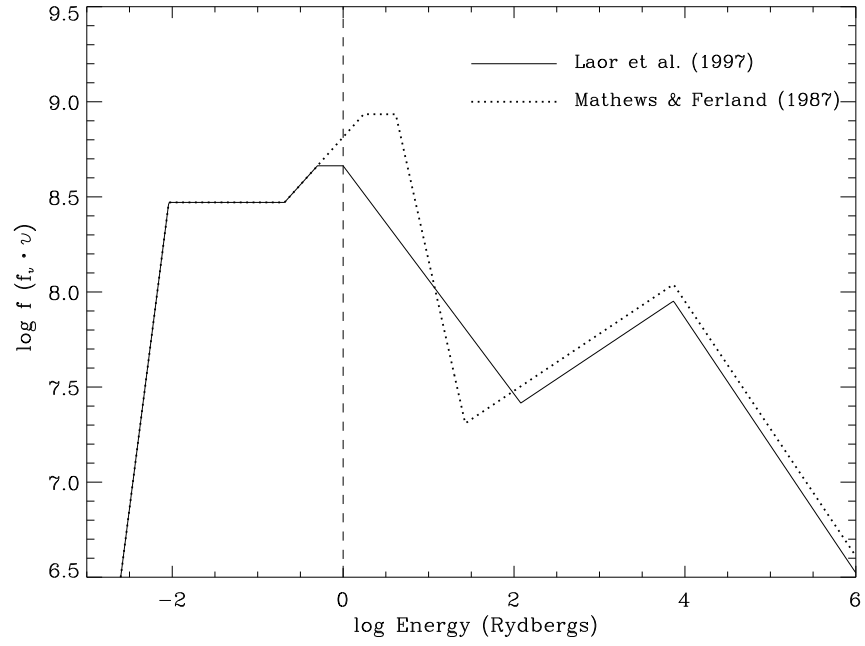


Fig. 15.— Spectral energy distribution used to compute the number of ionizing photons for Laor et al. (1997) in solid line and Mathews & Ferland (1987) in dotted line. Dashed line shows the Lyman limit.

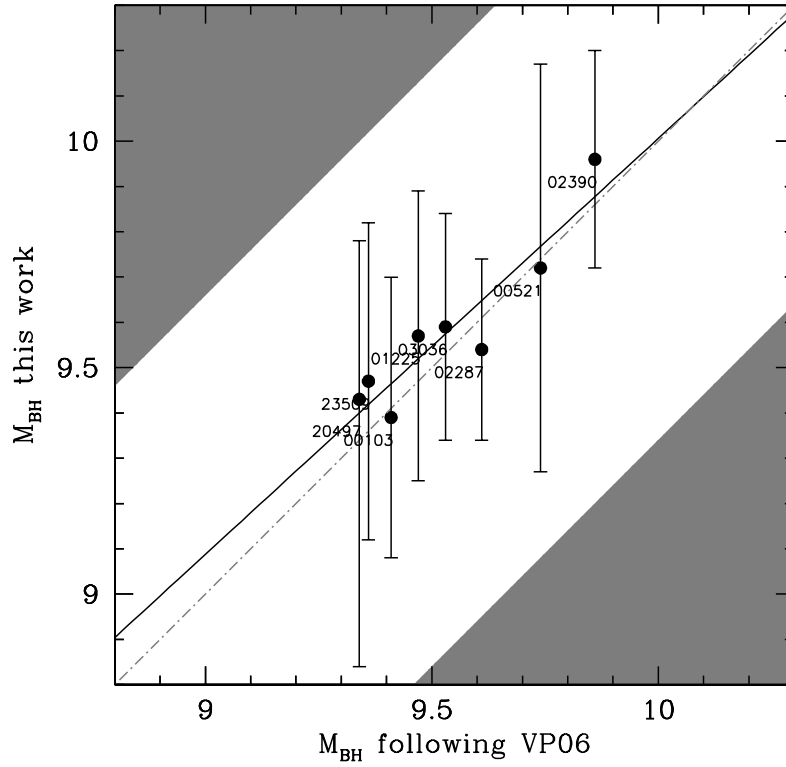


Fig. 16.— M_{BH} comparison. Abscissa and ordinate are logarithm of M_{BH} in solar masses. Each point is labeled with the object name in short format. In ordinate we report M_{BH} values obtained with the method of this paper; in abscissa those obtained employing the Vestergaard & Peterson relationship described in the text. The two “extreme” objects are not included. The shaded bands limit the 2σ confidence level spread expected on the basis of the Vestergaard & Peterson relationship.